Electronic Supplementary Material (ESI) for Catalysis Science & Technology.

Supplementary Information

Surface phase structures responsible for activity and deactivation of fcc MoC (111)-Mo surface in steam reforming: A systematic kinetic and thermodynamic investigation

Changqing Chu,*[a] Xue Liu,[b] Changning Wu,[a] Junguo Li [a] and Ke Liu*[ab]

[a.] Academy for Advanced Interdisciplinary Studies, Southern University of Science and Technology, Shenzhen 518055, China. E-mail: chucq@sustech.edu.cn

[b.] Department of Chemistry, Southern University of Science and Technology, Shenzhen 518055, China. E-mail: liuk@sustech.edu.cn.

List of methods details, Figures and Tables

Fig. S16 Configuration of O* adsorption (1/9 ML): top site configuration (a), cavity site configuration without second-layer C right below (b), and cavity site configuration with second-layer C right below (c). The relative stability of each configuration was represented by adsorption energy with ZPE correction and gaseous H_2O and H_2 as reference.

Fig. S17 Structure evolution of surface O* at 1/9 ML coverage with time scale of 1-1557 femtoseconds at temperature of 473.15K.

Fig. S18 Configurations of O* adsorption (1/9 ML) and adsorption energy without ZPE correction. Gaseous H_2 and H_2O as energy reference.

Fig. S19 Configurations of O* adsorption (2/9 ML) and adsorption energy without ZPE correction. Gaseous H_2 and H_2O as energy reference.

Fig. S20 Configurations of O* adsorption (1/3 ML) and adsorption energy without ZPE correction. Gaseous H_2 and H_2O as energy reference. (Only the representative and relatively stable structures are listed for clarity)

Fig. S21 Configurations of O* adsorption (4/9 ML) and adsorption energy without ZPE correction. Gaseous H_2 and H_2O as energy reference. (Only the representative and relatively stable structures are listed for clarity)

Fig. S22 Configurations of O* adsorption (5/9 ML) and adsorption energy without ZPE correction. Gaseous H_2 and H_2O as energy reference. (Only the representative and relatively stable structures are listed for clarity)

Fig. S23 Configurations of O* adsorption (2/3 ML) and adsorption energy without ZPE correction. Gaseous H_2 and H_2O as energy reference. (Only the representative and relatively stable structures are listed for clarity)

Fig. S24 Configurations of O* adsorption (7/9 ML) and adsorption energy without ZPE correction. Gaseous H_2 and H_2O as energy reference. (Only the representative and relatively stable structures are listed for clarity)

Fig. S25 Configurations of O* adsorption (8/9 ML) and adsorption energy without ZPE correction. Gaseous H_2 and H_2O as energy reference. (Only the representative and relatively stable structures are listed for clarity)

Fig. S26 Configurations of O* adsorption (1 ML) and adsorption energy without ZPE correction. Gaseous H_2 and H_2O as energy reference. (Only the representative and relatively stable structures are listed for clarity)

Fig. S27 The potential energy profiles with ZPE correction for H_2* dissociation at different coverages (Energies in eV with gaseous H_2O and H_2 as reference)

Fig. S28 Configurations of H* adsorption, average adsorption energies of H* and surface oxidation degree at different coverages on fcc MoC (111)-Mo surface. Gaseous H_2 as energy reference.

Fig. S29 Configurations of H_2* adsorption, average adsorption energies of H_2* and surface oxidation degree at different coverages on fcc MoC (111)-Mo surface. Gaseous H_2 as energy reference.

Fig. S30 Surface energy planes at 473.15K in (pH_2O, pH_2) space. In the partial pressure range of 10^{-3}—12 atm, the surface configurations of mixed OH*(2/3 ML) + H_2O*(1/3 ML), OH*(1/3 ML) + H_2O*(2/3 ML) and H_2O* (2/3 ML) are 16-27 kcal/mol, 46-69 kcal/mol and 109-166 kcal/mol less stable than the surface configuration of OH* (1 ML), respectively. It should to be noted here that H_2O* (2/3 ML) is the most stable configuration at the considered conditions.

Fig. S31 Surface energy planes at 473.15K in (pH_2O, pH_2) space. In the partial pressure range of 10^{-3}—12 atm, the surface configurations of mixed OH*(2/3 ML) + H_2*(1/3 ML) and H_2* (2/3 ML) are 51-107kcal/mol

and 60-208 kcal/mol less stable than the surface configuration of OH* (1 ML). It should to be noted here that H_2* (2/3 ML) is the most stable configuration in the vicinity of 1 atm.

Fig. S32 Surface energy planes at 473.15K in (pH_2O, pH_2) space. In the partial pressure range of 10^{-3}—12 atm, the surface configurations of mixed OH*(5/9 ML) + O*(4/9 ML), mixed OH*(2/3 ML) + O*(1/3 ML) and OH* (1 ML) are 13-32, 53-76 and 55-89 kcal/mol less stable than the surface configuration of O* (1 ML).

Fig. S33. Surface phase diagram of reactivity at 423.15K in (pH_2O, pH_2) space.

Fig. S34. Surface phase diagram of deactivation at 423.15K in (pH_2O, pH_2) space.

Fig. S35 Bilayer structure of H_2O adsorption (n = 9) on fcc MoC (111)-Mo terminated surface.

Fig. S36 CO oxidation to CO_2 on Pt/MoC (111)-Mo terminated surface by surface top site OH* (a) and by surface cavity site O* (b). The gas phase CO as energy scale reference, and energies in eV with ZPE corrections (blue ball for Mo, grey ball for C, red ball for O, white ball for H)

Table S1 Energetic aspects of surface H_2O^* dissociation with n adsorbing OH* (n = 1-3), $\Delta E_{TS,ZPE}^{\neq}$ and $\Delta E_{TS}^{\neq}$ were energy barriers of H_2O^* dissociation with or without ZPE correction, respectively; $\Delta E_{r,ZPE}$ and ΔE_r were reaction energies of H_2O^* dissociation with or without ZPE correction, respectively; σ_{TS}^{i} were imaginary frequencies of transition states for H_2O^* dissociation; $d_{O\cdots H}^{\neq}$ were the breaking O-H bond lengths of H_2O^* dissociation. Energies were in eV with H_2O^* adsorption states as reference, distances were in Å and frequencies were in cm^{-1}

Table S2 Energetic aspects of surface H_2O^* dissociation with n adsorbing O* (n = 1-3), $\Delta E_{TS,ZPE}^{\neq}$ and $\Delta E_{TS}^{\neq}$ were energy barriers of H_2O^* dissociation with or without ZPE correction, respectively; $\Delta E_{r,ZPE}$ and ΔE_r were reaction energies of H_2O^* dissociation with or without ZPE correction, respectively; σ_{TS}^{i} were imaginary frequencies of transition states for H_2O^* dissociation; $d_{O\cdots H}^{\neq}$ were the breaking O-H bond lengths of H_2O^* dissociation. Energies were in eV with H_2O^* adsorption states as reference, distances were in Å and frequencies were in cm^{-1}

Table S3 Energetic aspects of surface OH^* dissociation with n adsorbing O* (n = 1-3), $\Delta E_{TS,ZPE}^{\neq}$ and $\Delta E_{TS}^{\neq}$ were energy barriers of OH^* dissociation with or without ZPE correction, respectively; $\Delta E_{r,ZPE}$ and ΔE_r were reaction energies of OH^* dissociation with or without ZPE correction, respectively; σ_{TS}^{i} were imaginary frequencies of transition states for OH^* dissociation; $d_{O\cdots H}^{\neq}$ were the breaking O-H bond lengths of OH^* dissociation. Energies were in eV with OH^* adsorption states as reference, distances were in Å and frequencies were in cm^{-1}

Table S4 Energetic aspects of surface nH_2^* dissociation (n = 1-5), $\Delta E_{TS,ZPE}^{\neq}$ and $\Delta E_{TS}^{\neq}$ were energy barriers of nH_2^* dissociation with or without ZPE correction, respectively; $\Delta E_{r,ZPE}$ and ΔE_r were reaction energies of nH_2^* dissociation with or without ZPE correction, respectively; σ_{TS}^{i} were imaginary frequencies of transition states for nH_2^* dissociation; $d_{O\cdots H}^{\neq}$ were the breaking O-H bond lengths of nH_2^* dissociation. The configurations of transition states at increasing H_2^* coverage were listed below the table from left to right (the breaking and forming bonds were in yellow color). Energies were in eV with nH_2^* adsorption states as reference, distances were in Å and frequencies were in cm^{-1}

Table S5 The relative stability at 0K ($\Delta E_{AVG,n=1}^{i}$) for surface structures of H_2O^* (n = 1), OH* (n = 1), O* (n = 1), H* (n = 1) with respect to H_2* (n = 1) at increasing energy cutoff of 400, 450 and 500 eV. The differences of $\Delta E_{AVG,n=1}^{i}$ at 400 eV with those at 450 and 500 eV were also listed.

Table S6 Energetic aspects of surface OH* disproportionation, and energetic aspects of surface OH* direct deprotonation by surface Mo atoms.

S-1. Detailed description on the elementary reaction rate calculation

The reaction rate r of each elementary step in surface reactions is calculated as below:

$$r = \frac{k_B T}{h} \frac{q_{\mathrm{TS,vib}}}{q_{\mathrm{IS,vib}}} e^{-\frac{\mathrm{E_a}}{k_B T}}$$

Where k_B is Boltzmann constant, T denotes the reaction temperature, h is the Planck constant, Ea stands for the zero-point energy corrected energy barrier for elementary reaction derived from DFT calculations, $q_{TS,vib}$ and $q_{IS,vib}$ are the vibrational partition functions for the transition states and the initial states, respectively. q_{vib} is calculated as below:

$$q_{\mathrm{vib}} = \prod_i \frac{1}{1-e^{\frac{-h\nu_i}{k_B T}}}$$

where ν_i is the vibrational frequency of each vibrational mode of the surface adsorbing species derived from DFT harmonic frequency calculations. In order to cancel the error with low frequency mode, frequencies below 200 cm^{-1} were shifted to 200 cm^{-1}.

S-2. Detailed description on the *ab-initio* thermodynamic method

The stability of surface phase with i number adsorbing species at 0K without considering the temperature and pressure effects can be expressed as below:

$$\gamma_{0K} = E_{0K,ZPE}^{slab,adsorbates} - E_{0K}^{slab} - \sum_i (n_i * E_{0K,ZPE}^{i}) \qquad \text{(a)}$$

where $E_{0K,ZPE}^{slab,adsorbates}$ is the total energy of catalyst model with adsorbates (The ZPE corrections are included in the total energy of adsorbates), E_{0K}^{slab} is the total energy of clean catalyst model, $E_{0K,ZPE}^{i}$ is the total energy of isolated species i (The ZPE corrections are included in the total energy of isolated species), n_i is the number of adsorbing species i.

The stability of different surface configurations with i adsorbing species at temperature T and pressure p can be expressed as below:

$$\gamma_{\mathrm{T,p}} = G_{\mathrm{T,p}}^{slab,adsorbates} - G_{\mathrm{T,p}}^{slab} - \sum_i (n_i * \mu_{\mathrm{T,p}}^{i}) \qquad \text{(b)}$$

where $G_{\mathrm{T,p}}^{slab,adsorbates}$ is the Gibbs free energy of the catalyst model with adsorbates, $G_{\mathrm{T,p}}^{slab}$ is Gibbs free energy of the clean catalyst model, and $\mu_{\mathrm{T,p}}^{i}$ is the chemical potential of isolated species i. A more negative $\gamma_{\mathrm{T,p}}$ denotes a more stable surface structure. For the condensed phases, the variation of vibrational energy and entropy contributions to the Gibbs free energy usually cancel to a large extent in the subtraction term $G_{T,p}^{slab,adsorbates} - G_{T,p}^{slab}$, so Gibbs free energies $G_{T,p}^{slab,adsorbates}$ and $G_{T,p}^{slab}$ can be replaced by the total energies $E_{0K,ZPE}^{slab,adsorbates}$ and E_{0K}^{slab}, respectively. Thus equation (b) can be simplified as below:

$$\gamma_{T,p} = E_{0K,ZPE}^{slab,adsorbates} - E_{0K}^{slab} - \sum_i (n_i * \mu_{T,p}^{i}) \qquad \text{(c)}$$

Assuming isolated species as ideal gas, the chemical potential of species i depending on temperature and pressure can be expressed below:

$$\mu_{T,p}^{i} = E_{0K,ZPE}^{i} + \mu_{i,T}^{0} + \mathrm{RTln}(\frac{p^i}{p^0}) \qquad \text{(d)}$$

where $E_{0K,ZPE}^{i}$ is the total energy of isolated species i with ZPE correction obtained from DFT calculation, $\mu_{i,T}^{0}$ is the energy difference between the chemical potential (temperature T and pressure 1 atm) and total energy at 0K for species i, p^i is the partial pressure of species i, p^0 is the standard atmospheric pressure, $\mu_{i,T}^{0}$ values are taken from the JANAF thermochemical tables (https://janaf.nist.gov/).

Combining equation (a), (c) and (d), the following expression can be obtained:

$$\gamma_{T,p} = \gamma_{0K} - \sum_i (n_i * \mu_{i,T}^0) - RT \sum_i (n_i * \ln(\frac{p^i}{p^0})) \quad \text{(e)}$$

where the surface stability at 0K (represented by γ_{0K}) usually calculated by DFT calculations can be extended to realistic operating conditions (represented by $\gamma_{T,p}$).

The chemical potentials for surface adsorbing species (H_2O*, H_2*, OH*, O* and H*) are expressed below:

$$\mu_{T,p}^{H_2O} = E_{0K,ZPE}^{H_2O} + \mu_{H_2O,T}^0 + RT\ln(\frac{p^{H_2O}}{p^0});\ \mu_{T,p}^{H_2} = E_{0K,ZPE}^{H_2} + \mu_{H_2,T}^0 + RT\ln(\frac{p^{H_2}}{p^0});\ \mu_{T,p}^{OH} = \mu_{T,p}^{H_2O} - 0.5 * \mu_{T,p}^{H_2}$$

$$\mu_{T,p}^{O} = \mu_{T,p}^{H_2O} - \mu_{T,p}^{H_2};\ \mu_{T,p}^{H} = 0.5 * \mu_{T,p}^{H_2}$$

S-3. Detailed description on the definition of average adsorption energy

$$E_{AVG,n}^i = 1/n * (E_{0K,ZPE}^{slab,adsorbates} - E_{0K}^{slab} - n * E_{0K,ZPE}^i))$$

where $E_{0K,ZPE}^{slab,adsorbates}$ is the total energy of catalyst model with adsorbates (The ZPE corrections are included in the total energy of adsorbates), E_{0K}^{slab} is the total energy of clean catalyst model, $E_{0K,ZPE}^i$ is the total energy of isolated species i (The ZPE corrections are included in the total energy of isolated species), n_i is the number of adsorbing species i. The average adsorption energy of adsorbing species at different coverages (H_2O*, H_2*, OH*, O* and H*) are expressed below:

$$E_{AVG,n}^{H_2O} = 1/n * (E_{0K,ZPE}^{slab,n*H_2O} - E_{0K}^{slab} - n * E_{0K,ZPE}^{H_2O}))$$

$$E_{AVG,n}^{H_2} = 1/n * (E_{0K,ZPE}^{slab,n*H_2} - E_{0K}^{slab} - n * E_{0K,ZPE}^{H_2}))$$

$$E_{AVG,n}^{OH} = 1/n * (E_{0K,ZPE}^{slab,n*OH} - E_{0K}^{slab} - n * E_{0K,ZPE}^{H_2O} + n/2 * E_{0K,ZPE}^{H_2}))$$

$$E_{AVG,n}^{O} = 1/n * (E_{0K,ZPE}^{slab,n*O} - E_{0K}^{slab} - n * E_{0K,ZPE}^{H_2O} + n * E_{0K,ZPE}^{H_2}))$$

$$E_{AVG,n}^{H} = 1/n * (E_{0K,ZPE}^{slab,n*H} - E_{0K}^{slab} - n/2 * E_{0K,ZPE}^{H_2}))$$

S-4. Description on the procedure for searching the most stable sequential adsorption configurations

Here we take the searching procedure for OH* or O* as examples. As shown in Fig. 1, for the first adsorption (n = 1), there are only four possible sites in total for the trial configurations (top site configuration, bridge site configuration, cavity site configuration without second-layer C right below, and cavity site configuration with second-layer C right below). Then for each surface species, the above four possible configurations are all calculated by DFT ionic relaxations to evaluate the existence and total energies. For example, the OH* (n = 1) have the total four configurations as the minima at the PBE theory level (Fig. 3), whereas the O* (n = 1) only have three of them (Fig. S16). The relative stability of the surface species is computed and compared. The results show that the two cavity site configurations of OH* or O* are obviously much more stable than the other two configurations. (Fig. 3 and Fig. S16). Then actually we have four types of building blocks for OH* and three for O*. The building of the next configurations (n = 2 or higher) now focus on which type of the building blocks to choose and then where to place on the rest vacant sites. There are several rules which can help us to simplify the searching processes as follow:

1. The trial configurations at n (n is the number of adsorbing species) are only based on the configurations at n-1 with stability ranking high in the configurational list (In the current study, a threshold of 0.3 eV was

set, i.e. the configurations which are $\geq$0.3 eV less stable than the most stable structure, were not considered);

2. The building blocks of cavity site types are selected preferentially for the initial trials due to their much higher stability, and then certain proportion of cavity sites adsorbate are replaced by the top/bridge sites adsorbate to evaluate the mixed sites;

3. When placing building blocks at n > 1, the number of possible positions can be greatly reduced due to the positional equivalence by periodical boundary, by symmetry of surface configurations and by the chemical intuition. For example, if one O* is on a cavity site with second-layer C right below, then it is highly unstable to place another O* on the adjacent cavity site without second-layer C right below because of their short distances and thus resulted large electrostatic repulsion. For another example, the bridge site OH* and top site OH* usually can't stand alone, and they usually emerge in pairs with hydrogen bonds among them, which can greatly stabilize the surface.

4. The limiting cases are usually included in the researching scope, such as the surface covered with all top sites or cavity sites. For example, the surfaces covered with all top site OH* are highly unstable, whereas surfaces covered with all cavity site OH* at critical coverages are also highly unstable. The considerations on these limiting cases help us gain an overall sense and grasp on the configurational space sampling process.

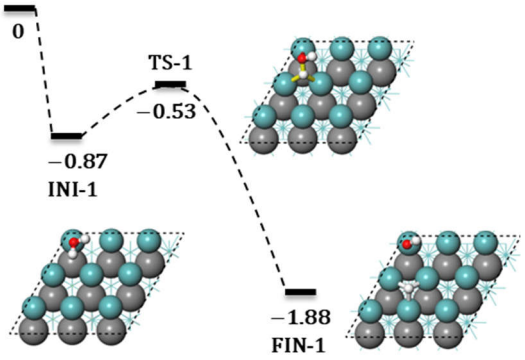
0
TS-1
−0.53
−0.87
INI-1
−1.88
FIN-1

(a)

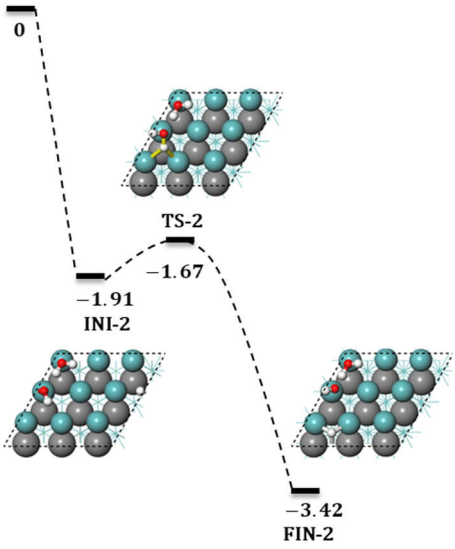
0
TS-2
−1.67
−1.91
INI-2
−3.42
FIN-2

(b)

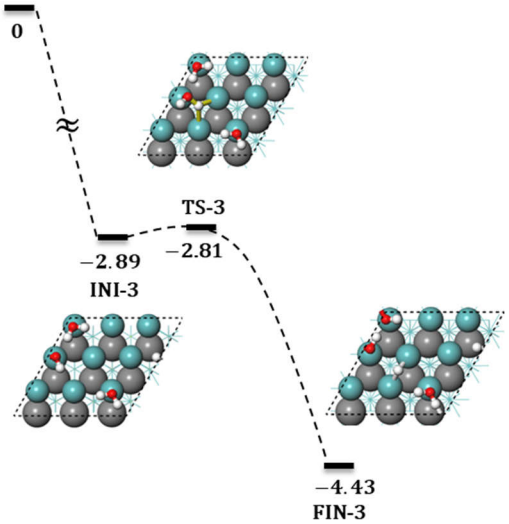
0
TS-3
−2.81
−2.89
INI-3
−4.43
FIN-3

(c)

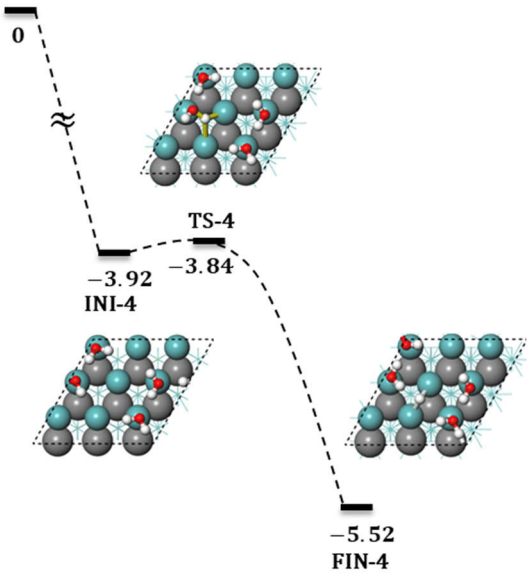
0
TS-4
−3.84
−3.92
INI-4
−5.52
FIN-4

(d)

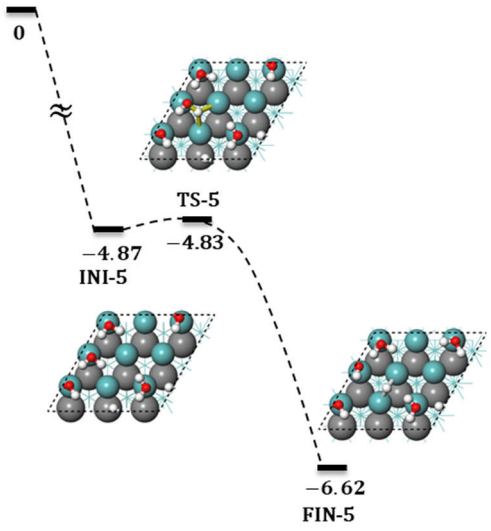
0
TS-5
−4.83
−4.87
INI-5
−6.62
FIN-5

(e)

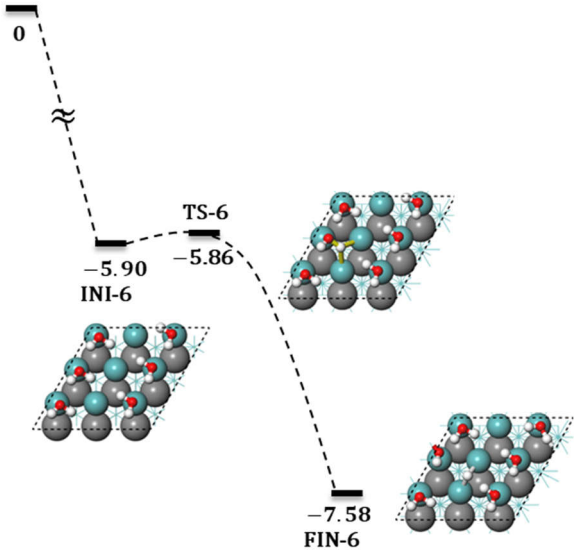
0
TS-6
−5.86
−5.90
INI-6
−7.58
FIN-6

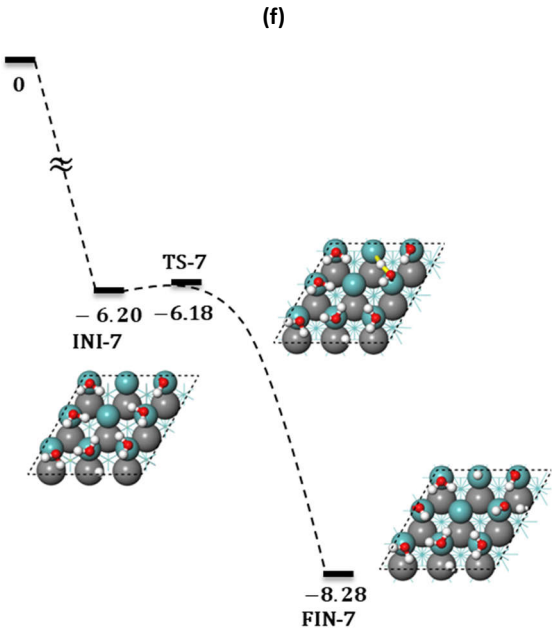

Fig. S1 The potential energy profiles with ZPE correction for H_2O dissociation at different coverages (Energies in eV with gaseous H_2O as reference)

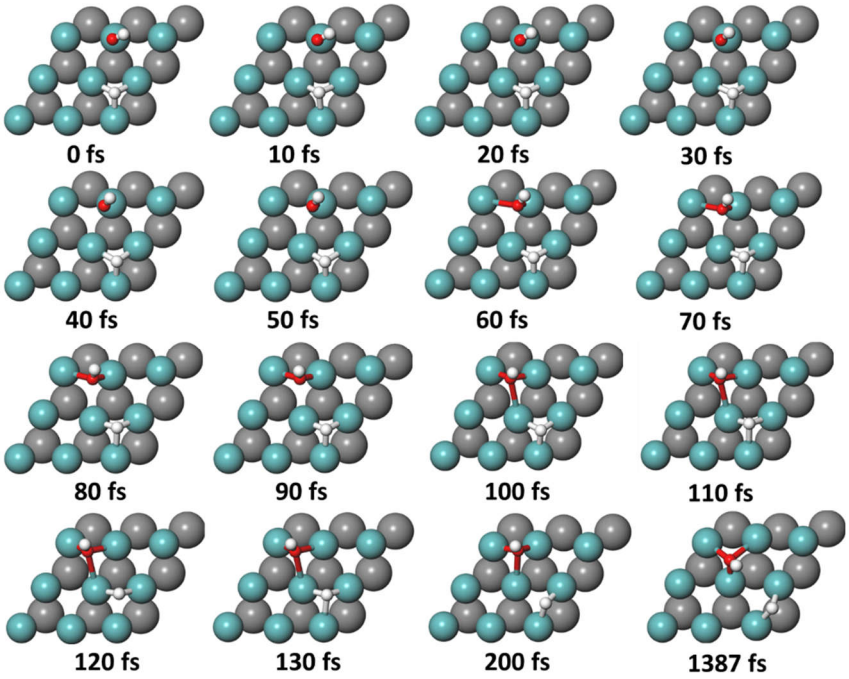

Fig. S2 Structure evolution of surface OH* at 1/9 ML coverage with time scale of 1-1387 femtoseconds at temperature of 473.15K.

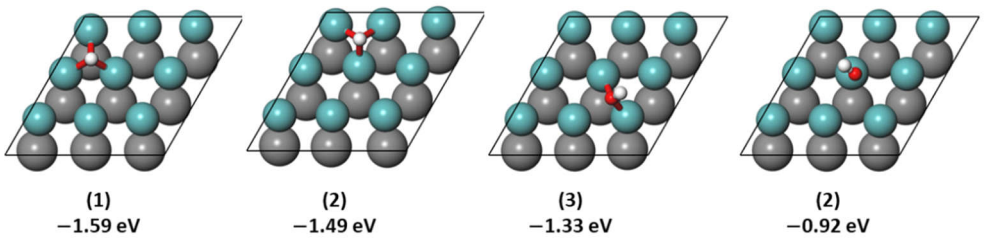

Fig. S3 Configurations of OH* adsorption (1/9 ML) and adsorption energy without ZPE correction. Gaseous H_2 and H_2O as energy reference.

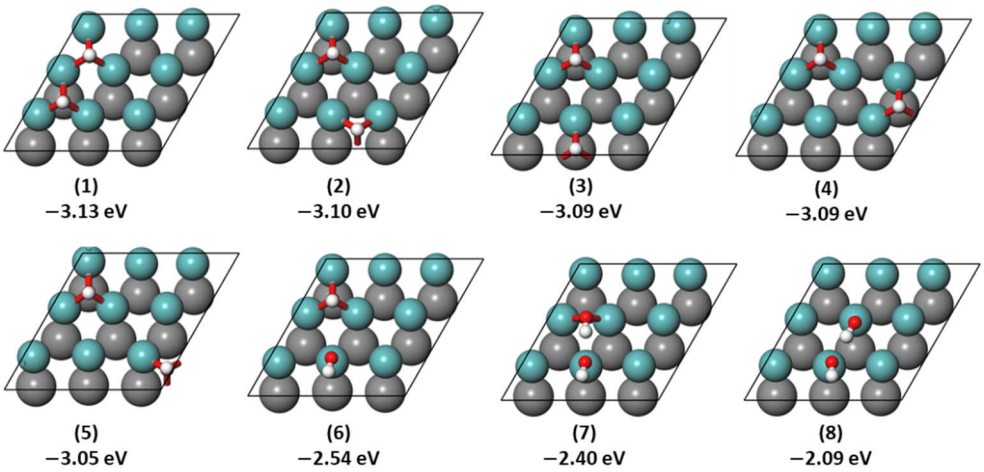

Fig. S4 Configurations of OH* adsorption (2/9 ML) and adsorption energy without ZPE correction. Gaseous H_2 and H_2O as energy reference.

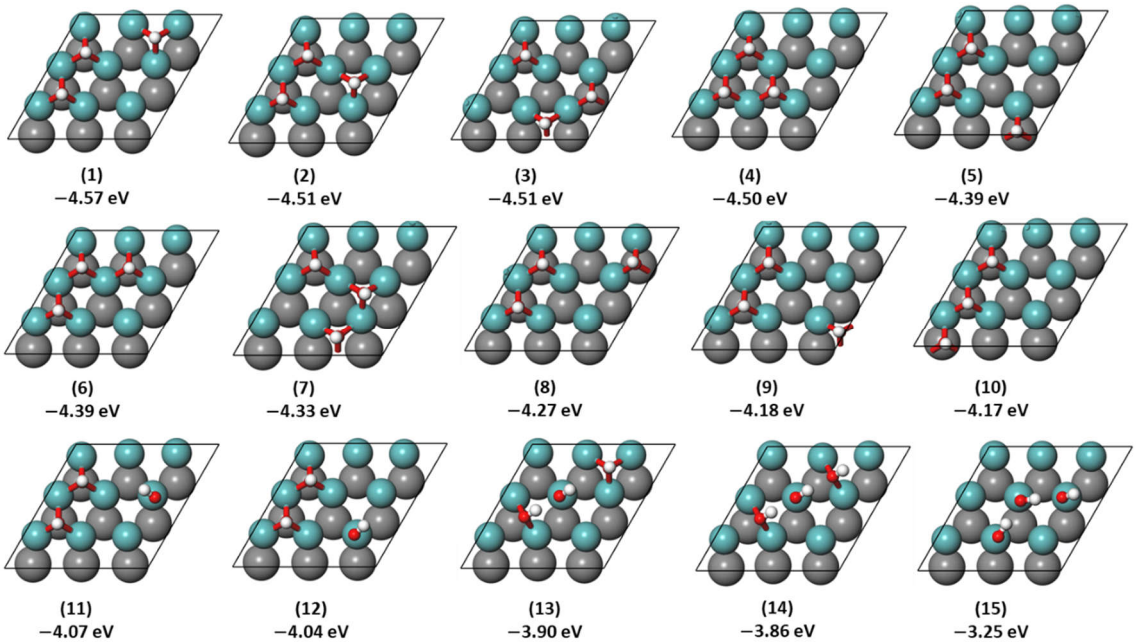

Fig. S5 Configurations of OH* adsorption (1/3 ML) and adsorption energy without ZPE correction. Gaseous H_2 and H_2O as energy reference. (Only the representative and relatively stable structures are listed for clarity)

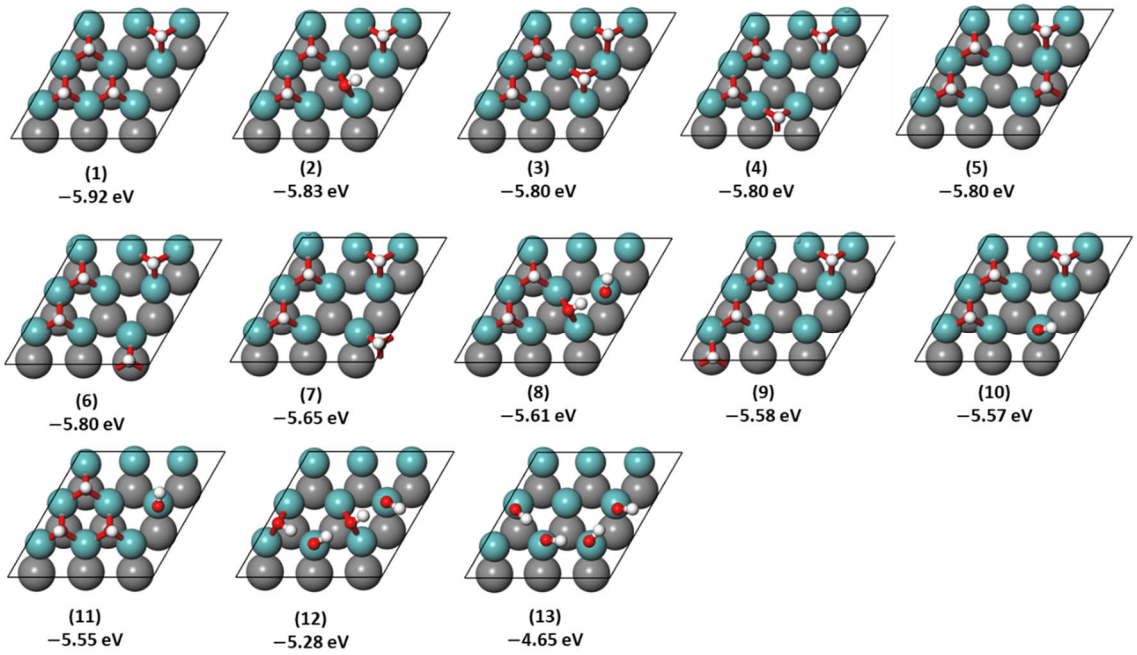

Fig. S6 Configurations of OH* adsorption (4/9 ML) and adsorption energy without ZPE correction. Gaseous H_2 and H_2O as energy reference. (Only the representative and relatively stable structures are listed for clarity)

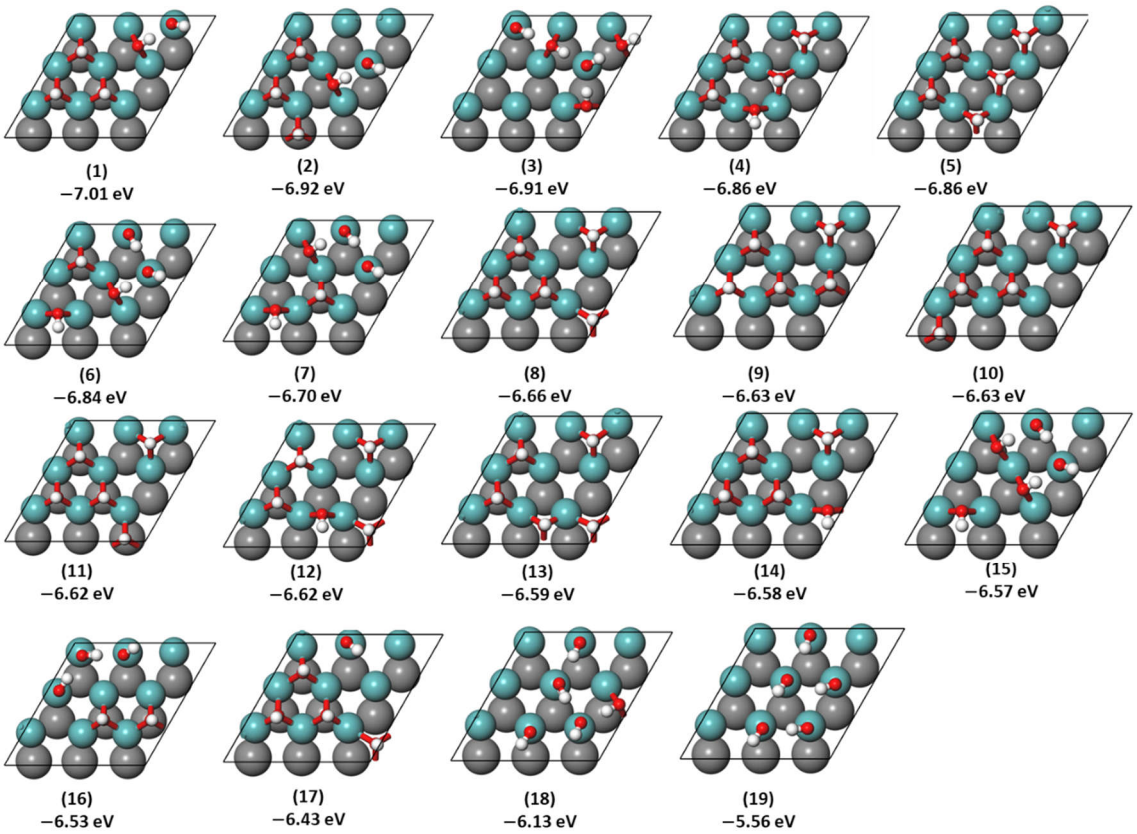

Fig. S7 Configurations of OH* adsorption (5/9 ML) and adsorption energy without ZPE correction. Gaseous H_2 and H_2O as energy reference. (Only the representative and relatively stable structures are listed for clarity)

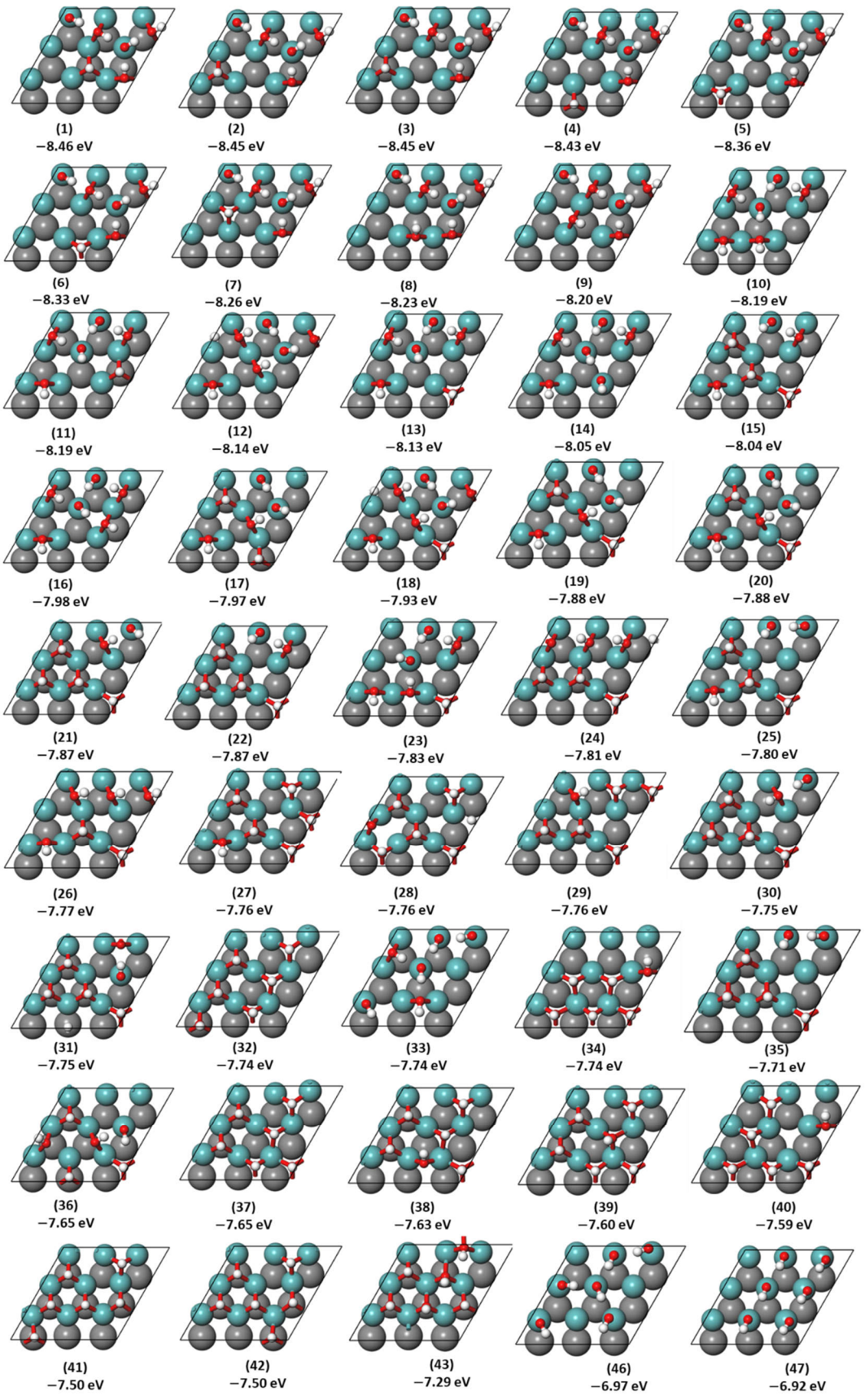
(1)
−8.46 eV
(2)
−8.45 eV
(3)
−8.45 eV
(4)
−8.43 eV
(5)
−8.36 eV
(6)
−8.33 eV
(7)
−8.26 eV
(8)
−8.23 eV
(9)
−8.20 eV
(10)
−8.19 eV
(11)
−8.19 eV
(12)
−8.14 eV
(13)
−8.13 eV
(14)
−8.05 eV
(15)
−8.04 eV
(16)
−7.98 eV
(17)
−7.97 eV
(18)
−7.93 eV
(19)
−7.88 eV
(20)
−7.88 eV
(21)
−7.87 eV
(22)
−7.87 eV
(23)
−7.83 eV
(24)
−7.81 eV
(25)
−7.80 eV
(26)
−7.77 eV
(27)
−7.76 eV
(28)
−7.76 eV
(29)
−7.76 eV
(30)
−7.75 eV
(31)
−7.75 eV
(32)
−7.74 eV
(33)
−7.74 eV
(34)
−7.74 eV
(35)
−7.71 eV
(36)
−7.65 eV
(37)
−7.65 eV
(38)
−7.63 eV
(39)
−7.60 eV
(40)
−7.59 eV
(41)
−7.50 eV
(42)
−7.50 eV
(43)
−7.29 eV
(46)
−6.97 eV
(47)
−6.92 eV

Fig. S8 Configurations of OH* adsorption (2/3 ML) and adsorption energy without ZPE correction. Gaseous H_2 and H_2O as energy reference. (Only the representative and relatively stable structures are listed for clarity)

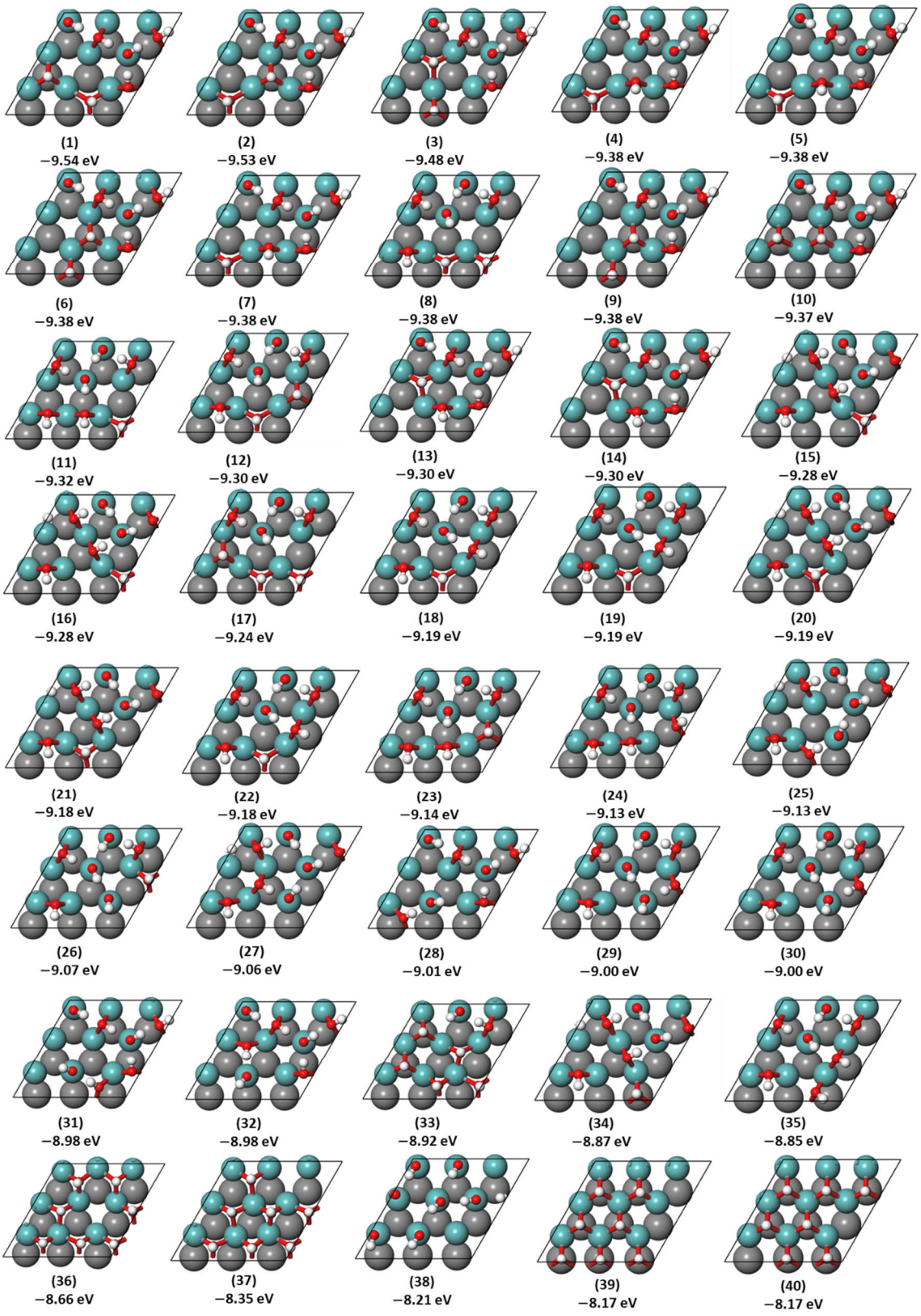

Fig. S9 Configurations of OH* adsorption (7/9 ML) and adsorption energy without ZPE correction. Gaseous H_2 and H_2O as energy reference. (Only the representative and relatively stable structures are listed for clarity)

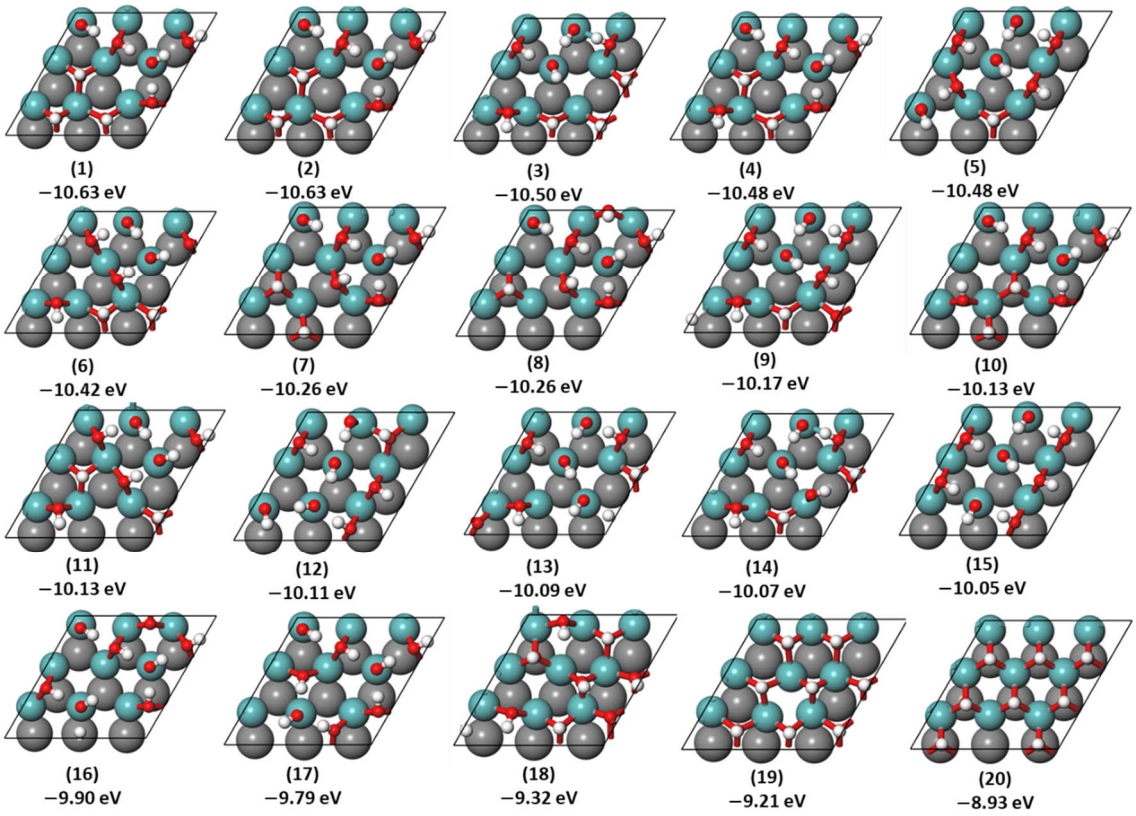

Fig. S10 Configurations of OH* adsorption (8/9 ML) and adsorption energy without ZPE correction. Gaseous H_2 and H_2O as energy reference. (Only the representative and relatively stable structures are listed for clarity)

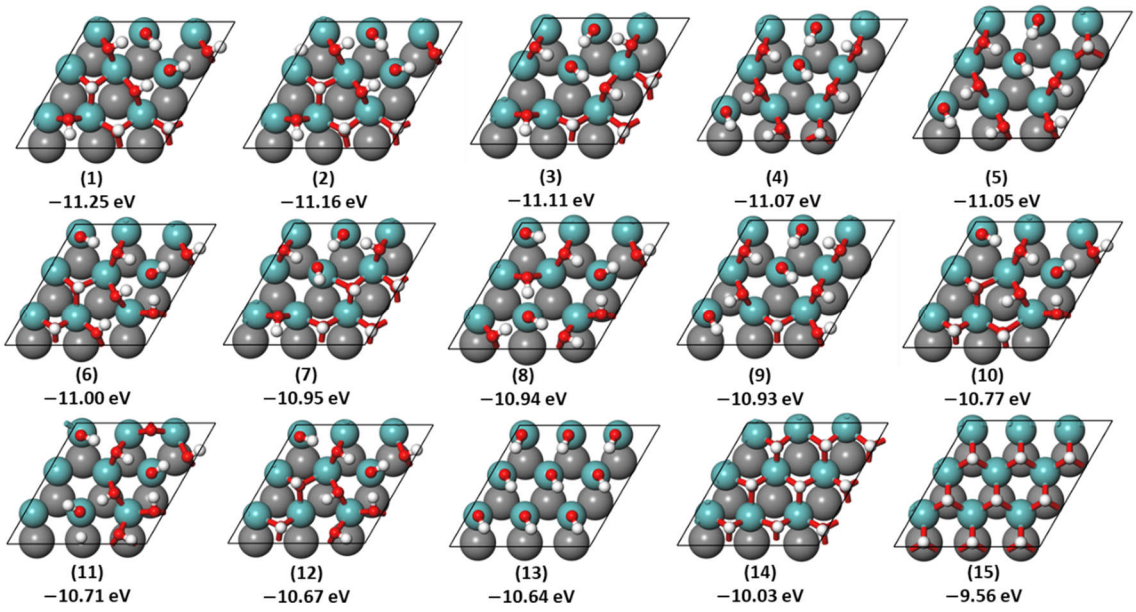

Fig. S11 Configurations of OH* adsorption (1 ML) and adsorption energy without ZPE correction. Gaseous H_2 and H_2O as energy reference. (Only the representative and relatively stable structures are listed for clarity)

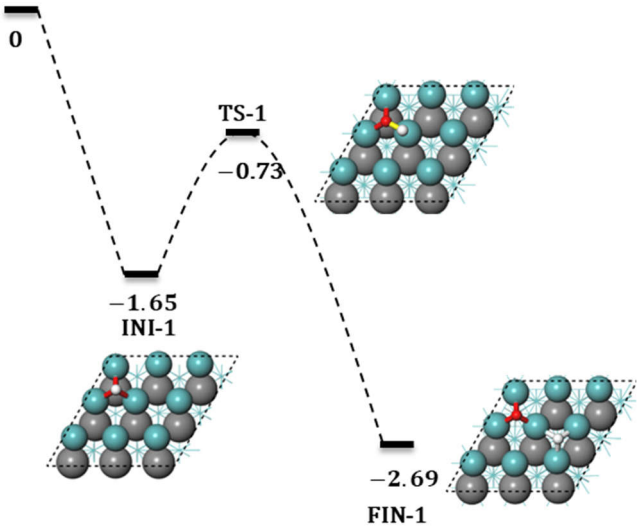
0
TS-1
−0.73
−1.65
INI-1
−2.69
FIN-1

(a)

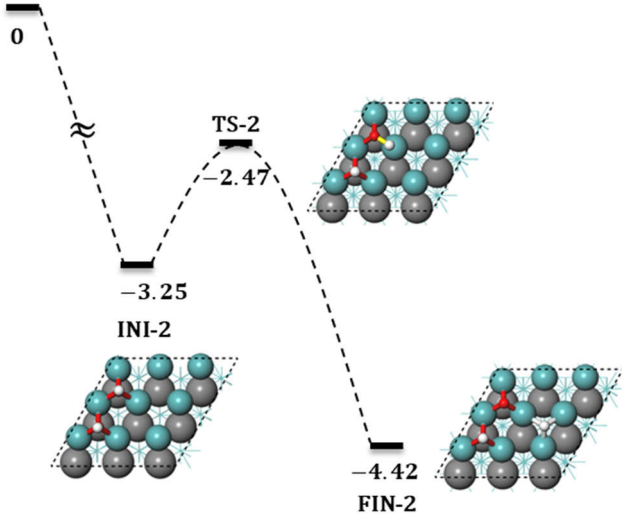
0
TS-2
−2.47
−3.25
INI-2
−4.42
FIN-2

(b)

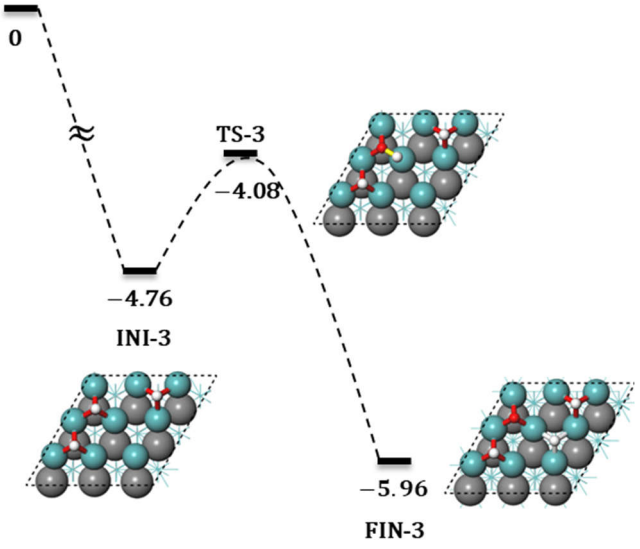
0
TS-3
−4.08
−4.76
INI-3
−5.96
FIN-3

(c)

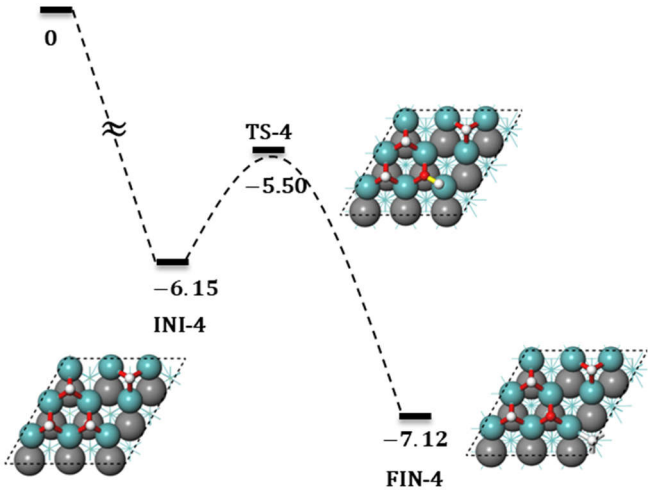
0
TS-4
−5.50
−6.15
INI-4
−7.12
FIN-4

(d)

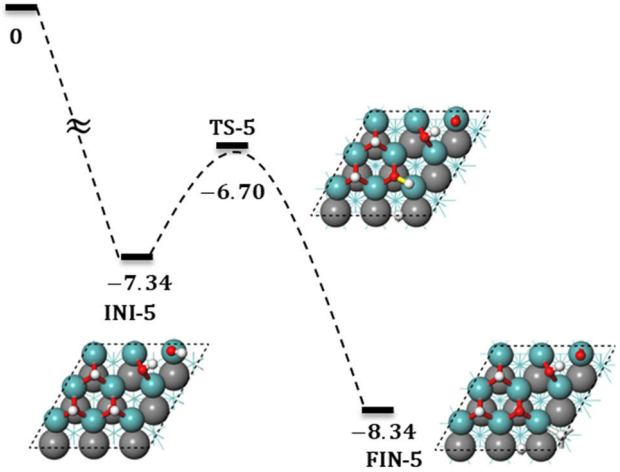
0
TS-5
−6.70
−7.34
INI-5
−8.34
FIN-5

(e)

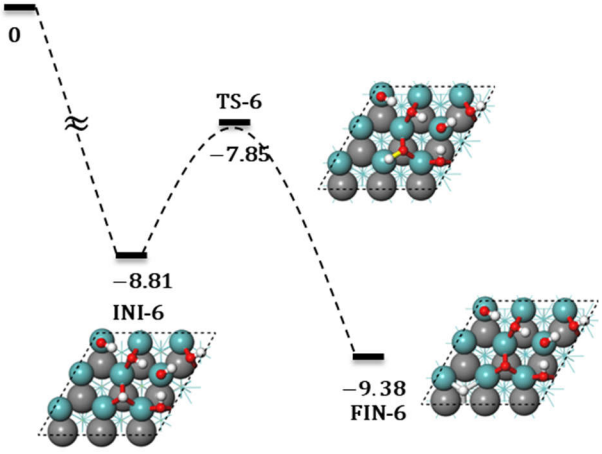
0
TS-6
−7.85
−8.81
INI-6
−9.38
FIN-6

(f)

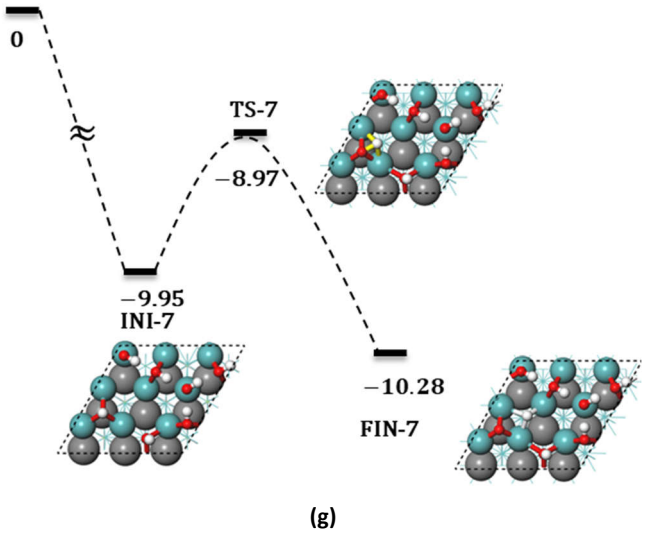

Fig. S12 The potential energy profiles with ZPE correction for OH* dissociation at different coverages (Energies in eV with gaseous H_2O and H_2 as reference)

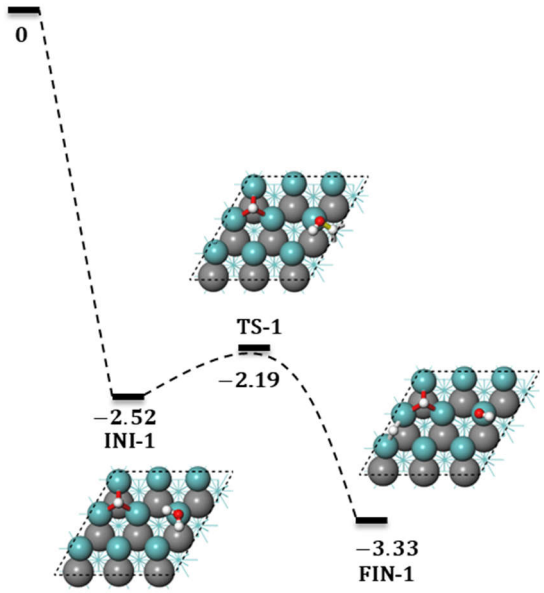

(a)

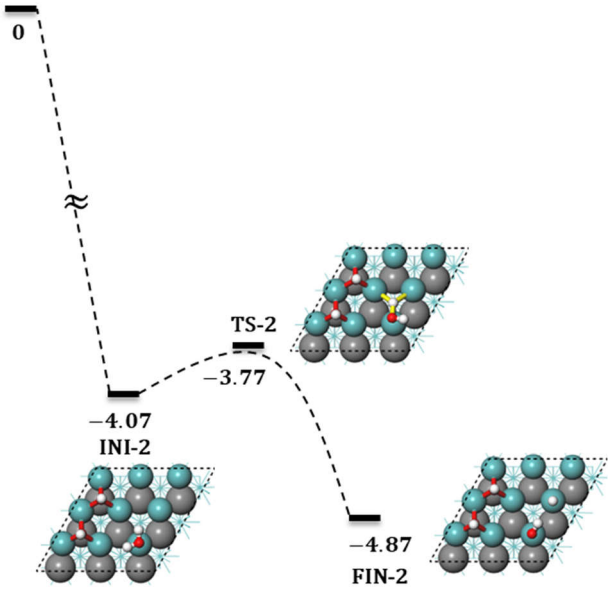

(b)

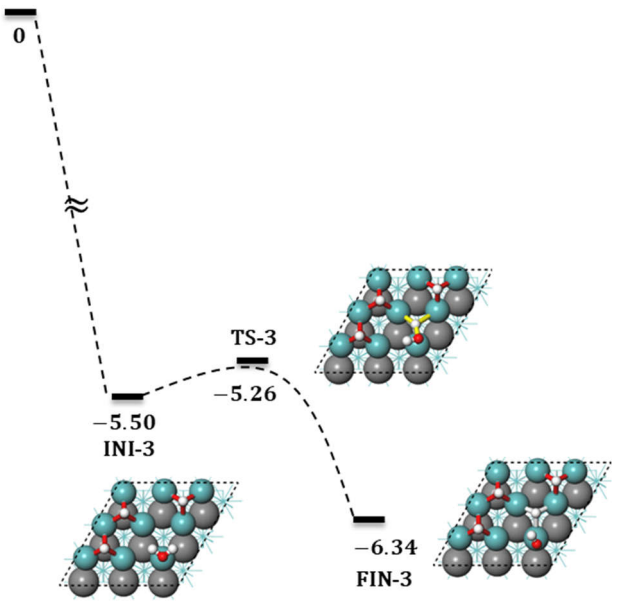

(c)

Fig. S13 The potential energy profiles with ZPE correction for H_2O* dissociation with n adsorbing OH* (n=1-3, energies in eV with gaseous H_2O and H_2 as reference)

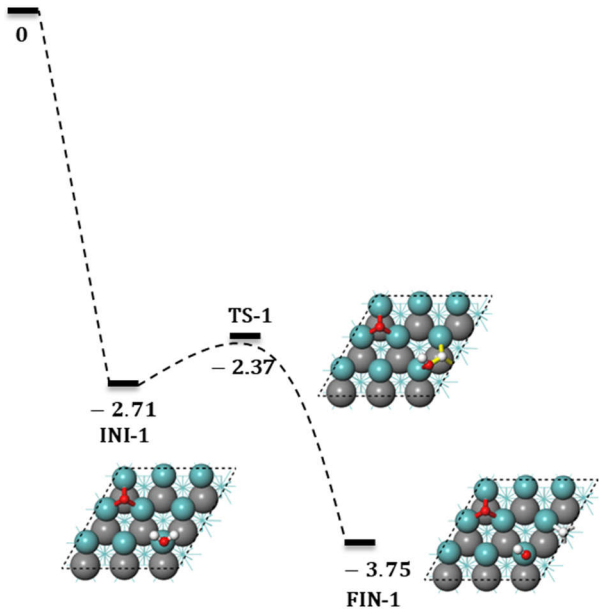

(a)

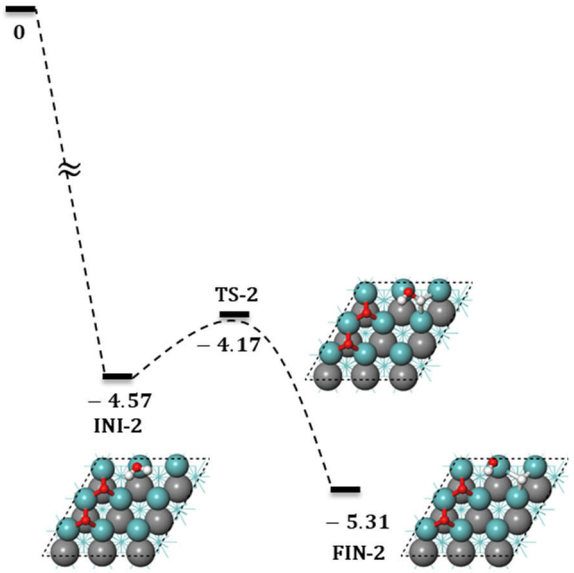

(b)

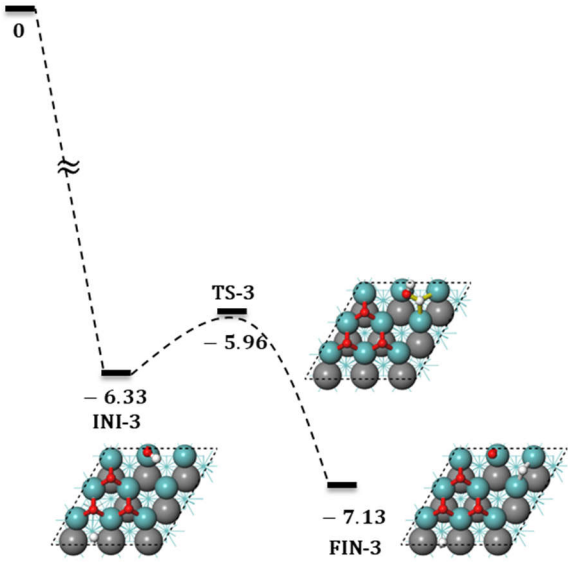

(c)

Fig. S14 The potential energy profiles with ZPE correction for H_2O* dissociation with n adsorbing O* (n=1-3, energies in eV with gaseous H_2O and H_2 as reference)

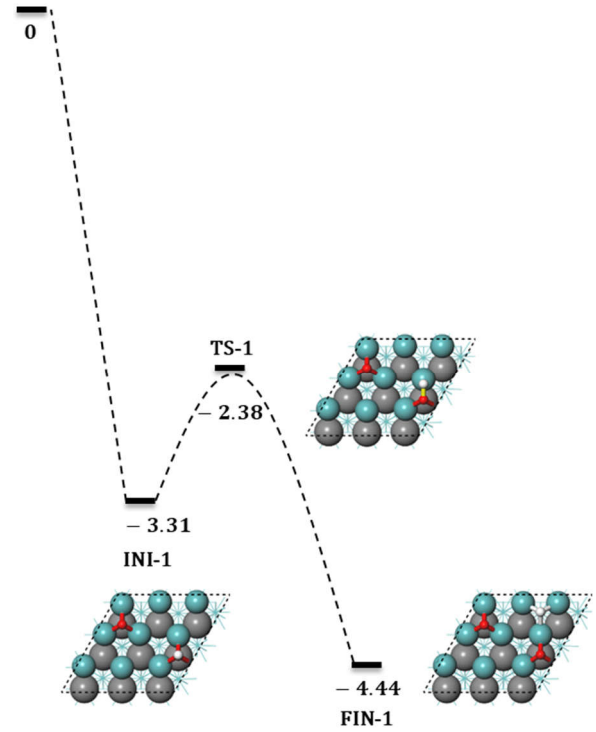

(a)

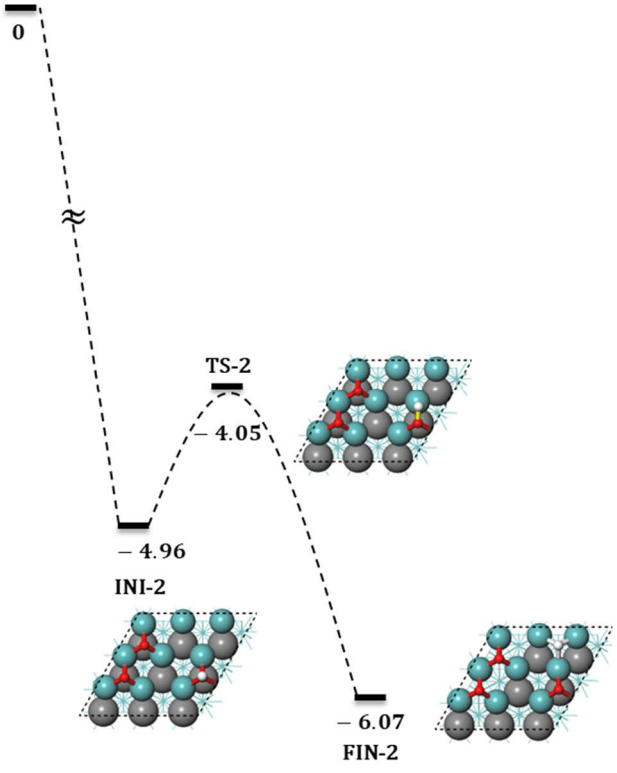

(b)

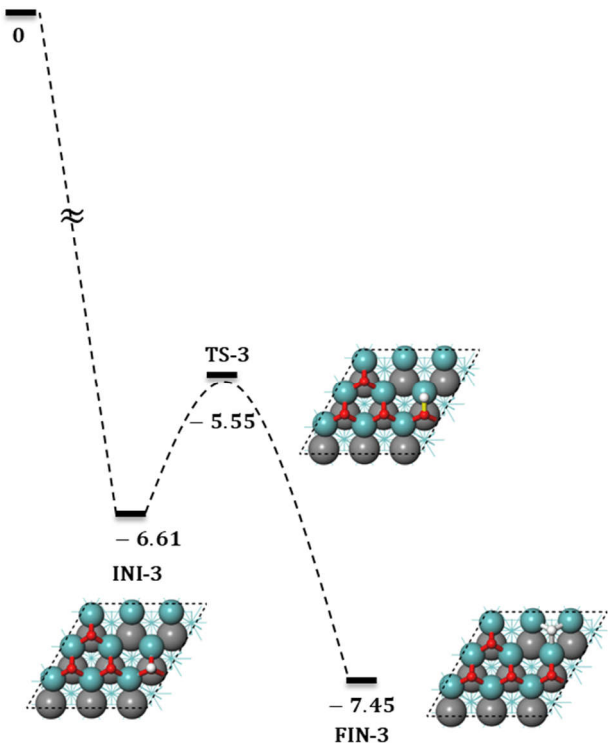

(c)

Fig. S15 The potential energy profiles with ZPE correction for OH* dissociation with n adsorbing O* (n=1-3, energies in eV with gaseous H_2O and H_2 as reference)

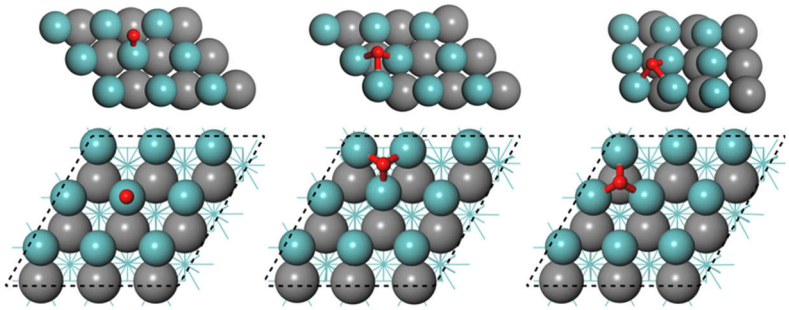

Fig. S16 Configuration of O* adsorption (1/9 ML): top site configuration (a), cavity site configuration without second-layer C right below (b), and cavity site configuration with second-layer C right below (c). The relative stability of each configuration was represented by adsorption energy with ZPE correction with gaseous H_2O and H_2 as reference.

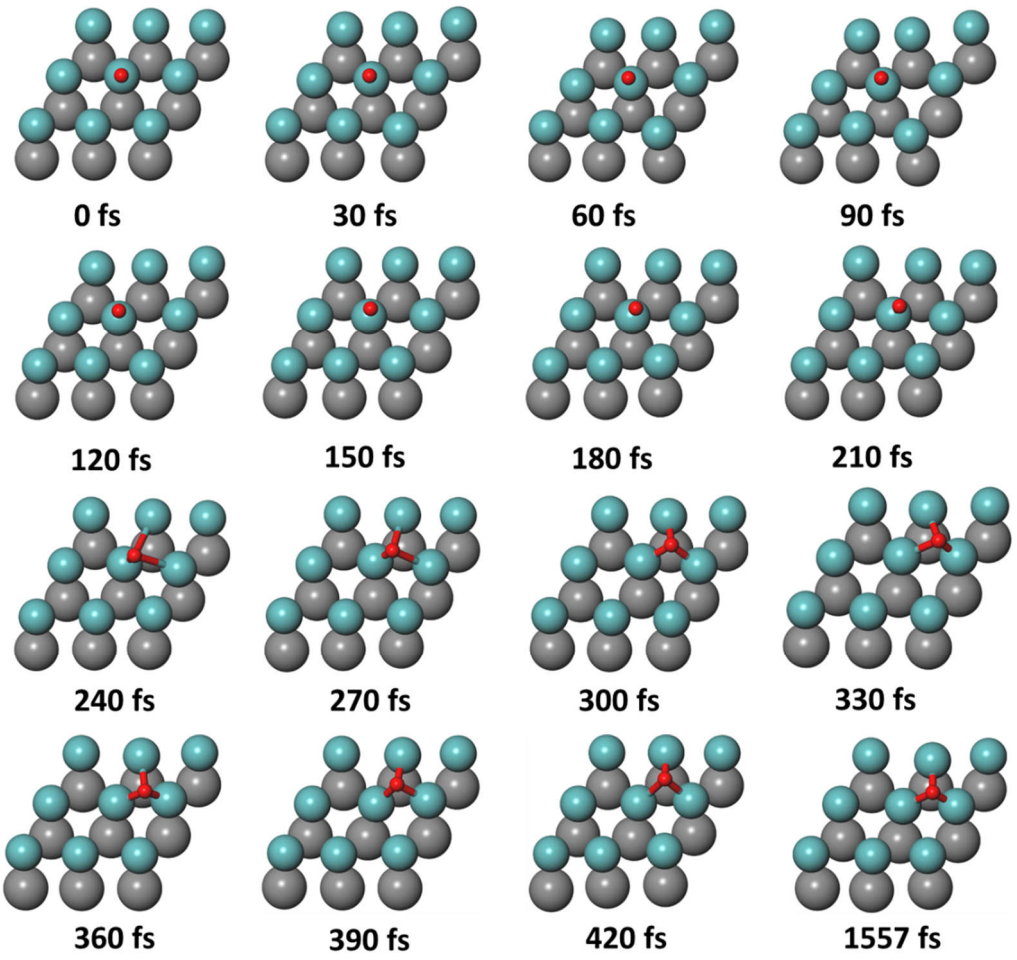

Fig. S17 Structure evolution of surface O* at 1/9 ML coverage with time scale of 1-1557 femtoseconds at temperature of 473.15K.

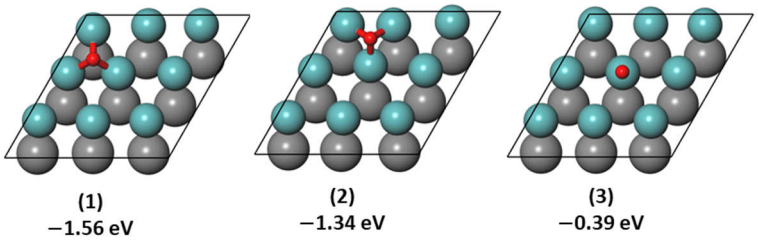

Fig. S18 Configurations of O* adsorption (1/9 ML) and adsorption energy without ZPE correction. Gaseous H_2 and H_2O as energy reference.

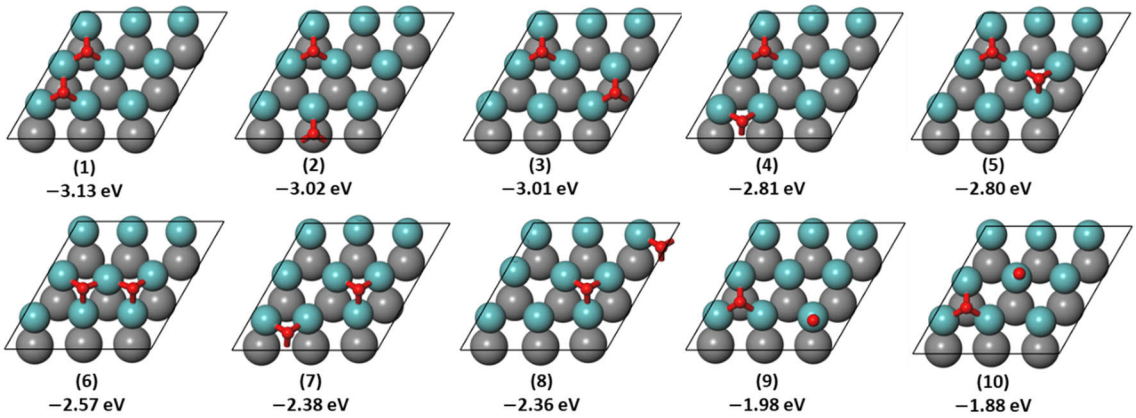

Fig. S19 Configurations of O* adsorption (2/9 ML) and adsorption energy without ZPE correction. Gaseous H_2 and H_2O as energy reference.

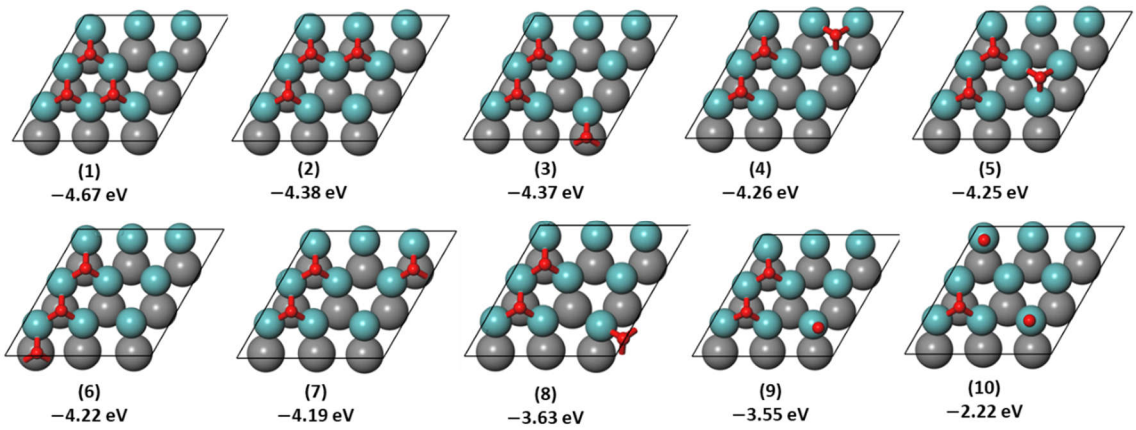

Fig. S20 Configurations of O* adsorption (1/3 ML) and adsorption energy without ZPE correction. Gaseous H_2 and H_2O as energy reference. (Only the representative and relatively stable structures are listed for clarity)

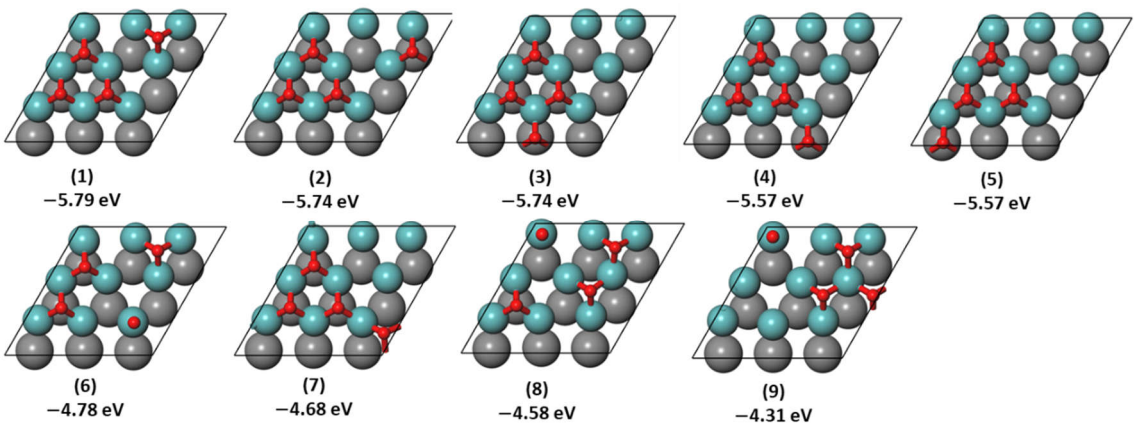

Fig. S21 Configurations of O* adsorption (4/9 ML) and adsorption energy without ZPE correction. Gaseous H_2 and H_2O as energy reference. (Only the representative and relatively stable structures are listed for clarity)

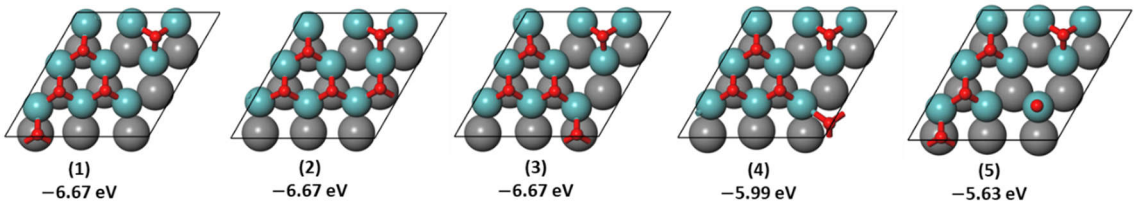

Fig. S22 Configurations of O* adsorption (5/9 ML) and adsorption energy without ZPE correction. Gaseous H_2 and H_2O as energy reference. (Only the representative and relatively stable structures are listed for clarity)

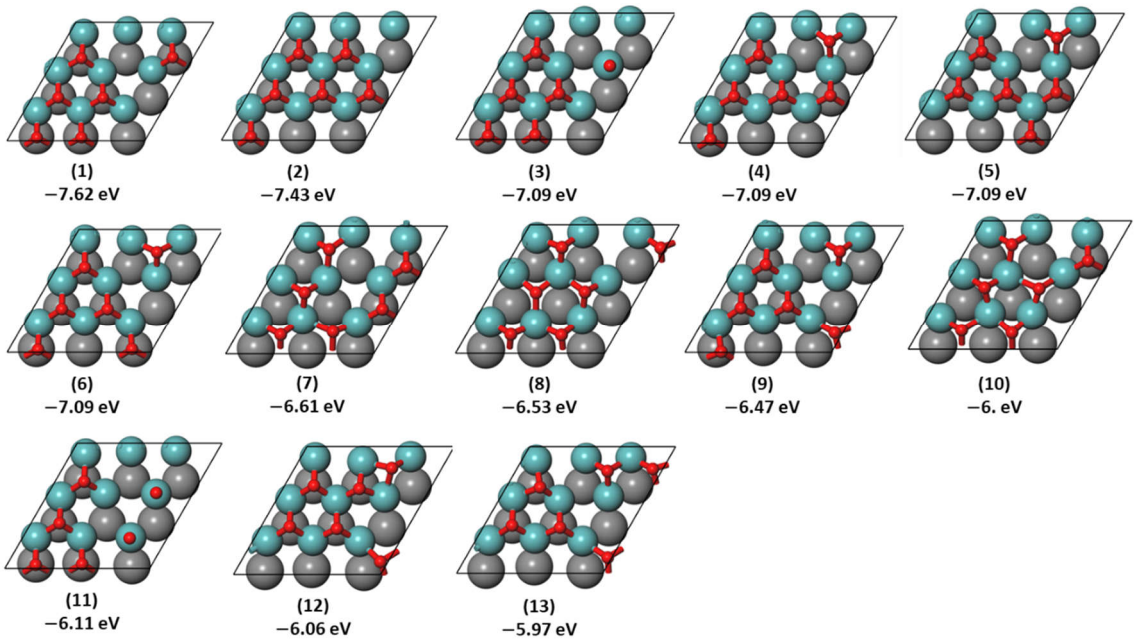

Fig. S23 Configurations of O* adsorption (2/3 ML) and adsorption energy without ZPE correction. Gaseous H_2 and H_2O as energy reference. (Only the representative and relatively stable structures are listed for clarity)

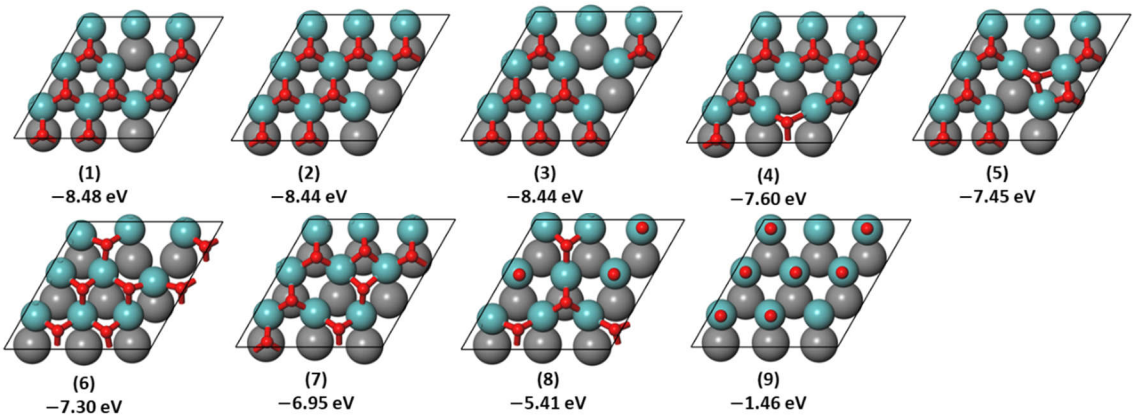

Fig. S24 Configurations of O* adsorption (7/9 ML) and adsorption energy without ZPE correction. Gaseous H_2 and H_2O as energy reference. (Only the representative and relatively stable structures are listed for clarity)

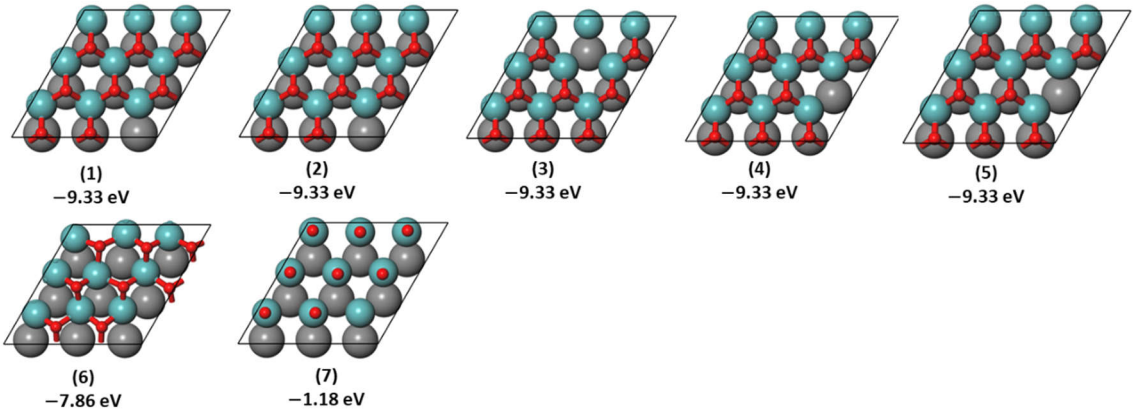

Fig. S25 Configurations of O* adsorption (8/9 ML) and adsorption energy without ZPE correction. Gaseous H_2 and H_2O as energy reference. (Only the representative and relatively stable structures are listed for clarity)

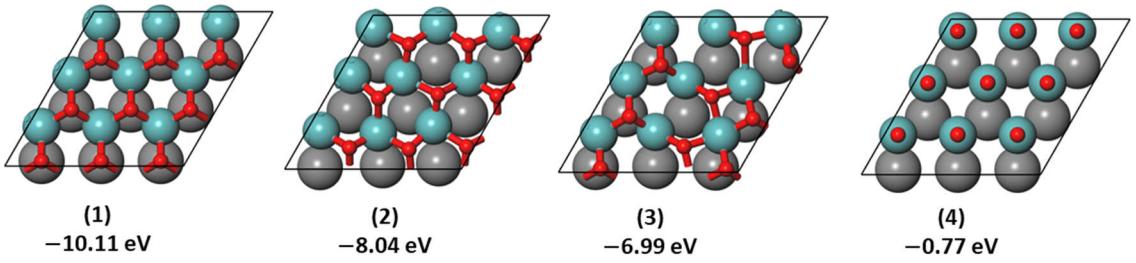

Fig. S26 Configurations of O* adsorption (1 ML) and adsorption energy without ZPE correction. Gaseous H_2 and H_2O as energy reference. (Only the representative and relatively stable structures are listed for clarity)

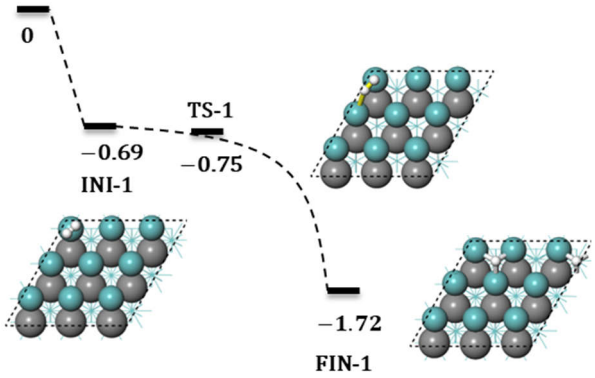
0
TS-1
−0.69
INI-1
−0.75
−1.72
FIN-1

(a)

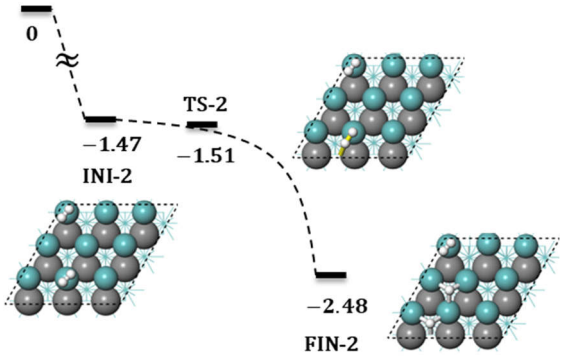
0
TS-2
−1.47
INI-2
−1.51
−2.48
FIN-2

(b)

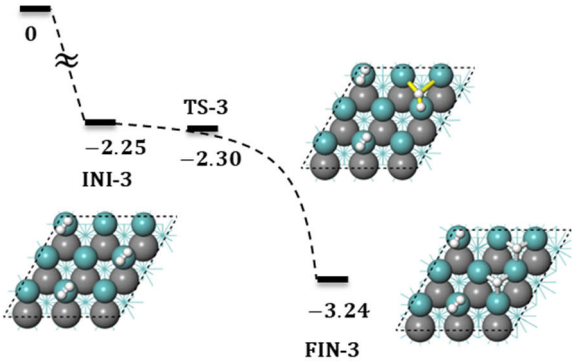
0
TS-3
−2.25
INI-3
−2.30
−3.24
FIN-3

(c)

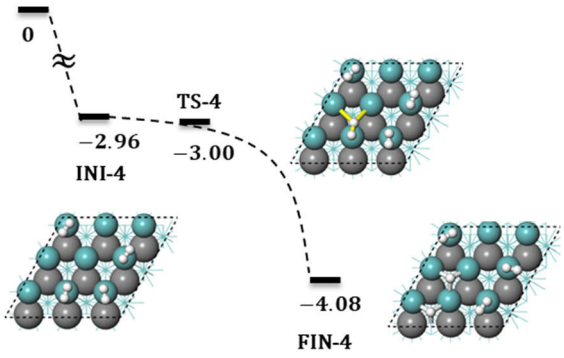
0
TS-4
−2.96
INI-4
−3.00
−4.08
FIN-4

(d)

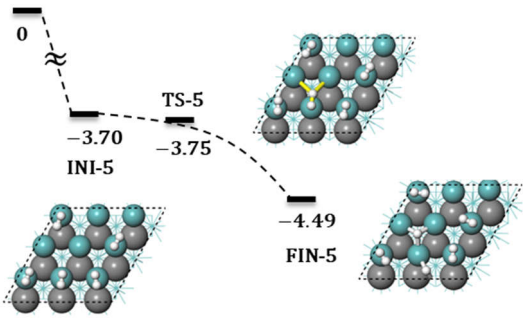

(e)

Fig. S27 The potential energy profiles with ZPE correction for H_2* dissociation at different coverages (Energies in eV with gaseous H_2 as reference). The slightly negative energy barriers were due to ZPE corrections.

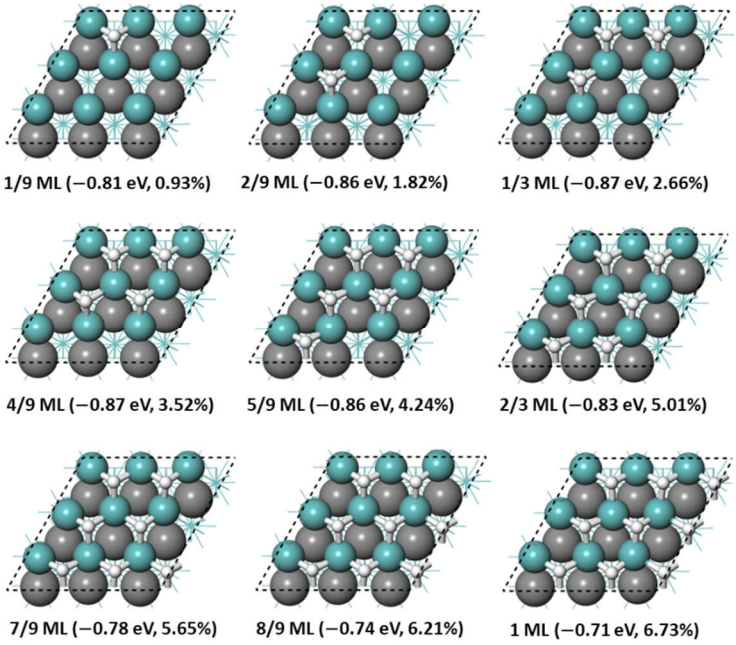

Fig. S28 Configurations of H* adsorption, average adsorption energies of H* and surface oxidation degree at different coverages on fcc MoC (111)-Mo surface. Gaseous H_2 as energy reference.

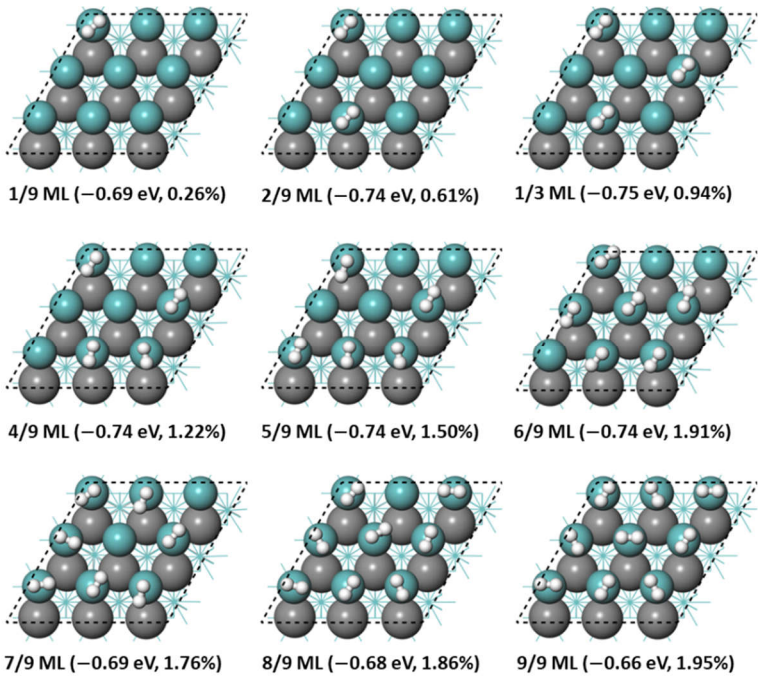

Fig. S29 Configurations of H_2* adsorption, average adsorption energies of H_2* and surface oxidation degree at different coverages on fcc MoC (111)-Mo surface. Gaseous H_2 as energy reference.

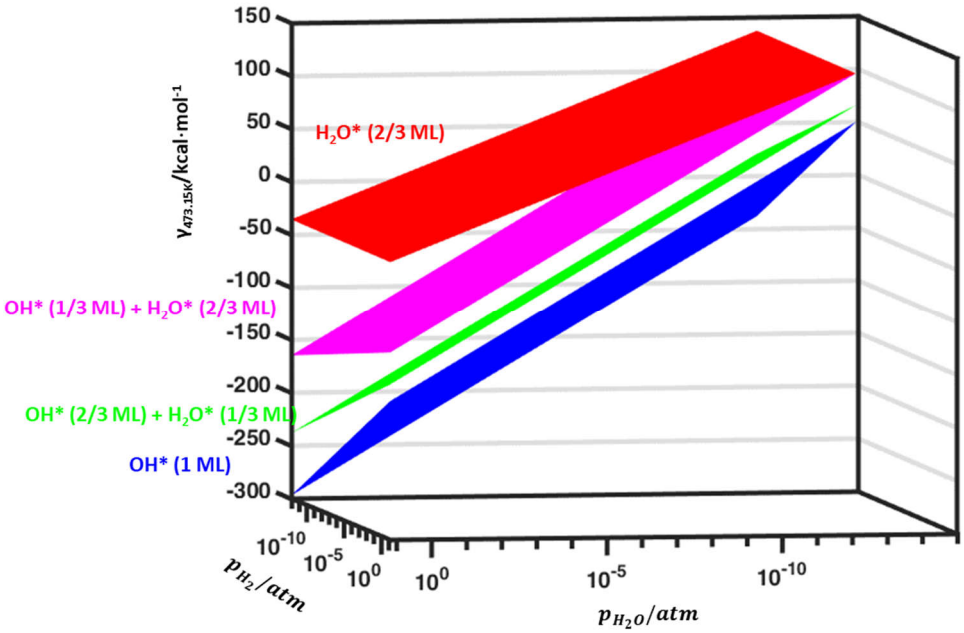

Fig. S30 Surface energy planes at 473.15K in (pH_2O, pH_2) space. In the partial pressure range of 10^{-3}—12 atm, the surface configurations of mixed OH*(2/3 ML) + H_2O*(1/3 ML), OH*(1/3 ML) + H_2O*(2/3 ML) and H_2O* (2/3 ML) are 16-27 kcal/mol, 46-69 kcal/mol and 109-166 kcal/mol less stable than the surface configuration of OH* (1 ML), respectively. It should to be note here that H_2O* (2/3 ML) is the most stable configuration at the considered conditions.

As shown in Fig. S30, the surface energies of the mixtures of OH* (n = 6) + H_2O* (n = 3), OH* (n = 3) + H_2O*

(n = 6) and H_2O^* (n = 6) were 16 – 27 kcal/mol, 46 – 69 kcal/mol and 109 – 166 kcal/mol less stable than the surface configurations of OH* (n = 9), indicating that the more amount of OH* replaced by H_2O^* only lead to less stable surface configurations. It should to be noted that H_2O^*（n = 6）is the most stable configuration among all coverages of H_2O adsorption (n = 1 – 9) at the above considered conditions.

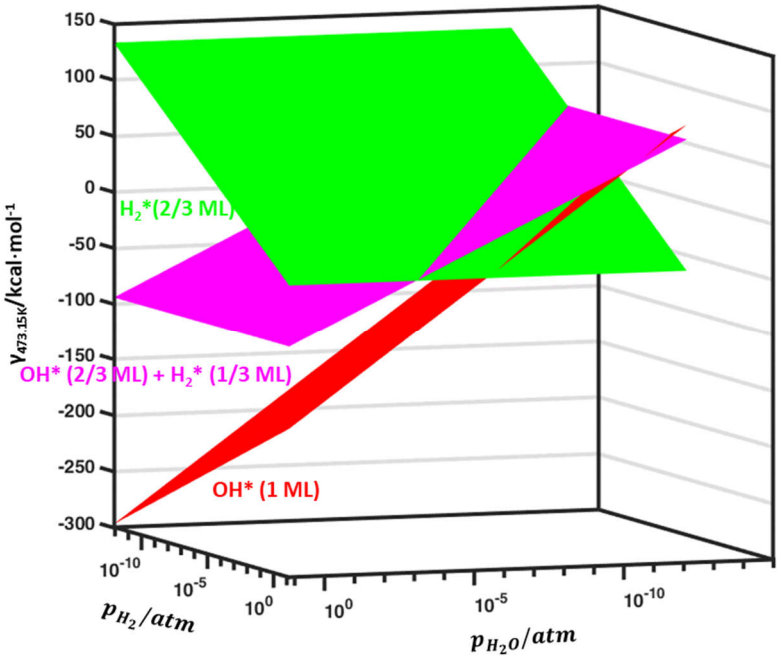

Fig. S31 Surface energy planes at 473.15K in (pH_2O, pH_2) space. In the partial pressure range of 10^{-3}—12 atm, the surface configurations of mixed OH*(2/3 ML) + H_2*(1/3 ML) and H_2* (2/3 ML) are 51-107kcal/mol and 60-208 kcal/mol less stable than the surface configuration of OH* (1 ML).

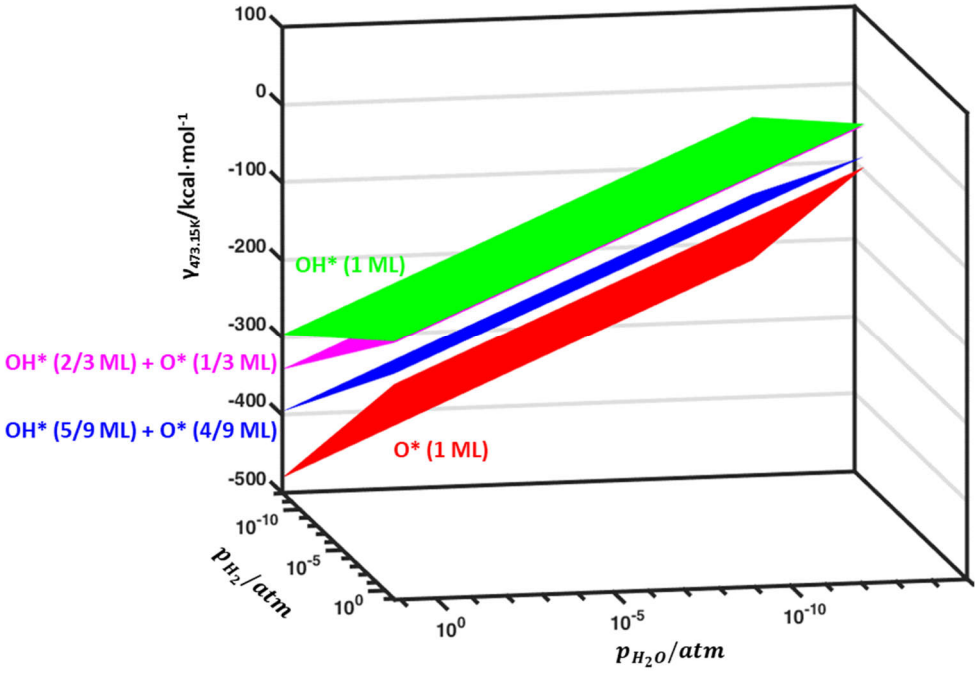

Fig. S32 Surface energy planes at 473.15K in (pH_2O, pH_2) space. In the partial pressure range of 10^{-3}—12 atm, the surface configurations of mixed OH*(5/9 ML) + O*(4/9 ML), mixed OH*(2/3 ML) + O*(1/3 ML) and OH* (1 ML) are 13-32, 53-76 and 55-89 kcal/mol less stable than the surface configuration of O* (1 ML).

As shown in Fig. S32, the surface configurations of mixed OH* (n = 5) + O* (n = 4), mixed OH* (n = 6) + O* (n = 3) and OH* (n = 9) are 13 – 32, 53 – 76 and 55 – 89 kcal/mol less stable than the surface configuration of O* (n = 9), indicating that the more amount of O* replaced by OH* only lead to less stable surface configurations. By combining the results of Fig. S30 and Fig. S32, the surface stabilities are in the order of pure O* > mixed O* + OH* > pure OH* > mixed OH* + H_2O* > pure H_2O*, and we can safely infer that the mixture of O* + H_2O* would always lead to less stable surface configurations with respect to pure O* in the considered conditions.

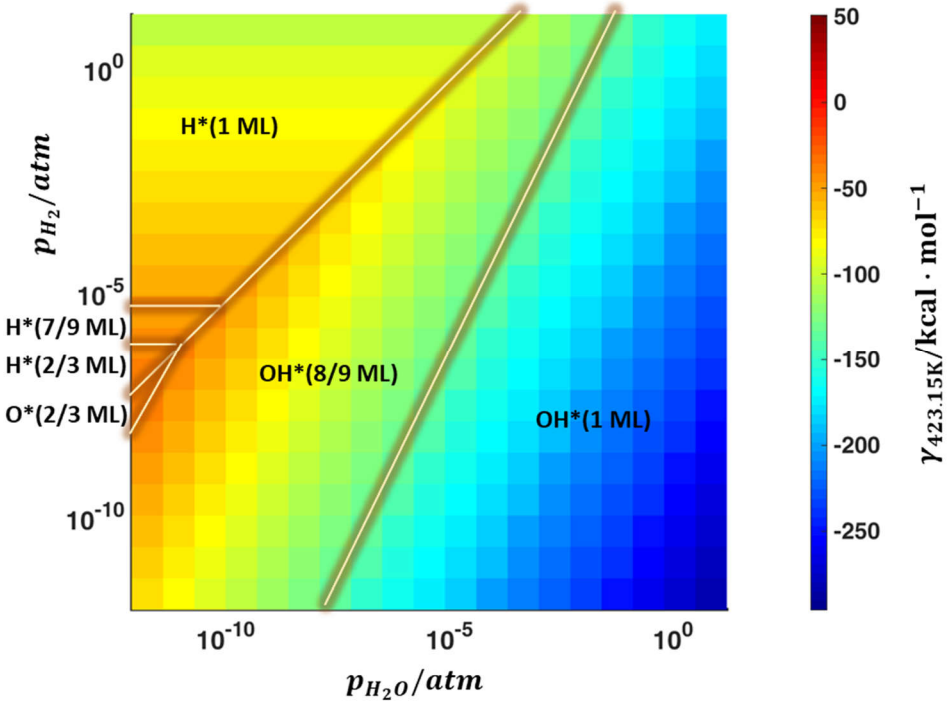

Fig. S33 Surface phase diagram of reactivity at 423.15K in (pH_2O, pH_2) space.

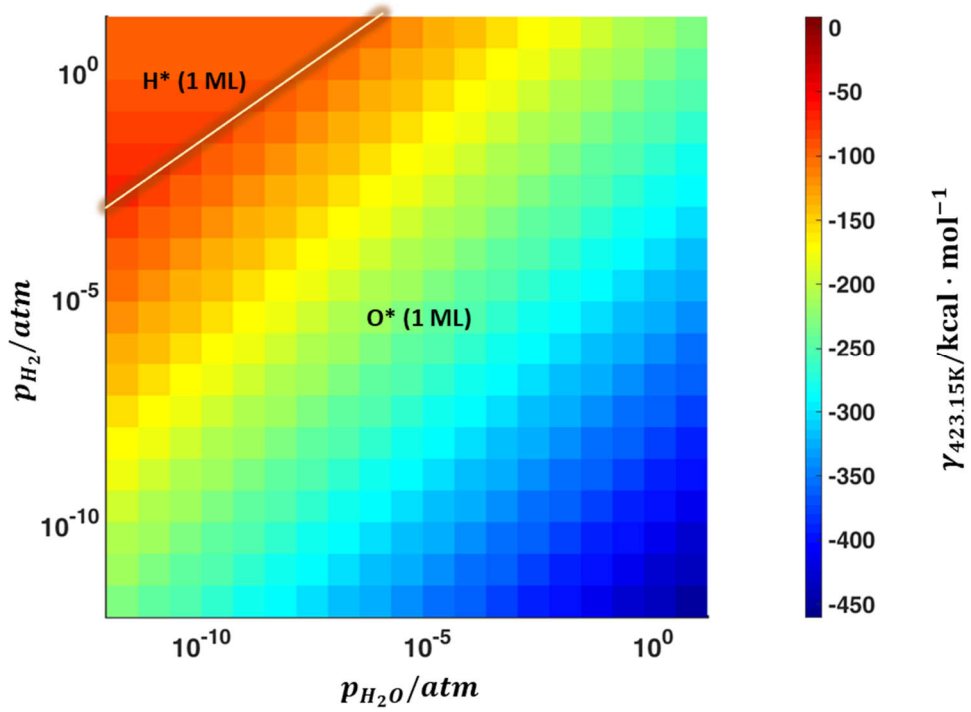

Fig. S34 Surface phase diagram of deactivation at 423.15K in (pH_2O, pH_2) space.

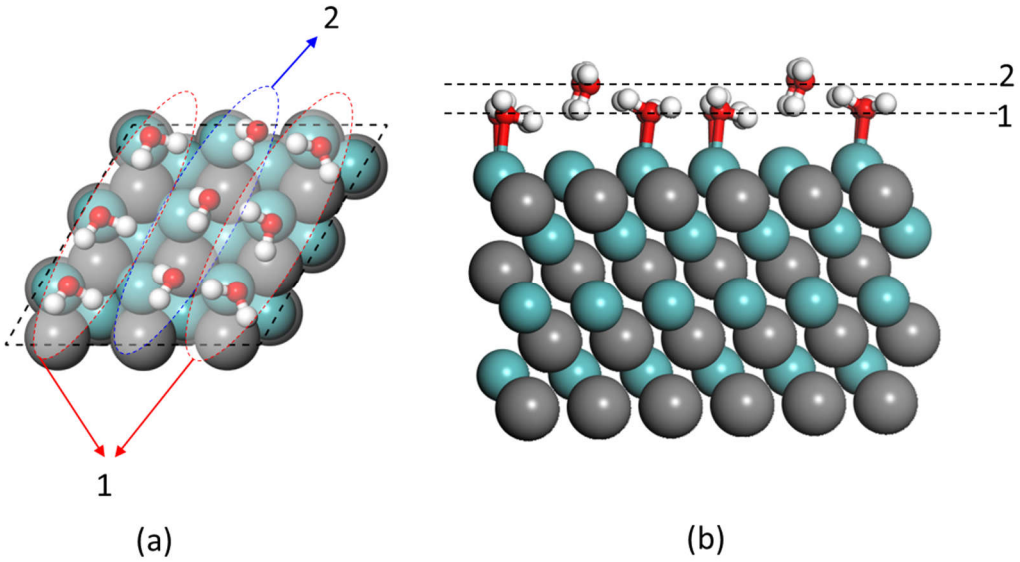

Fig. S35 Bilayer structure of H_2O adsorption (n = 9) on fcc MoC (111)-Mo terminated surface. (a) the top view; (b) the side view. (green ball for Mo, grey ball for C, red ball for O, white ball for H)

As shown in **Fig. S35**, the adsorption structures denoted by 1 were the stable adsorption configurations at $n \leq 6$, while the structures denoted by 2 emerged at $n \geq 7$, the structures of which resembled the buckled H-down configuration in the bilayer structure on Rh (111) surface.

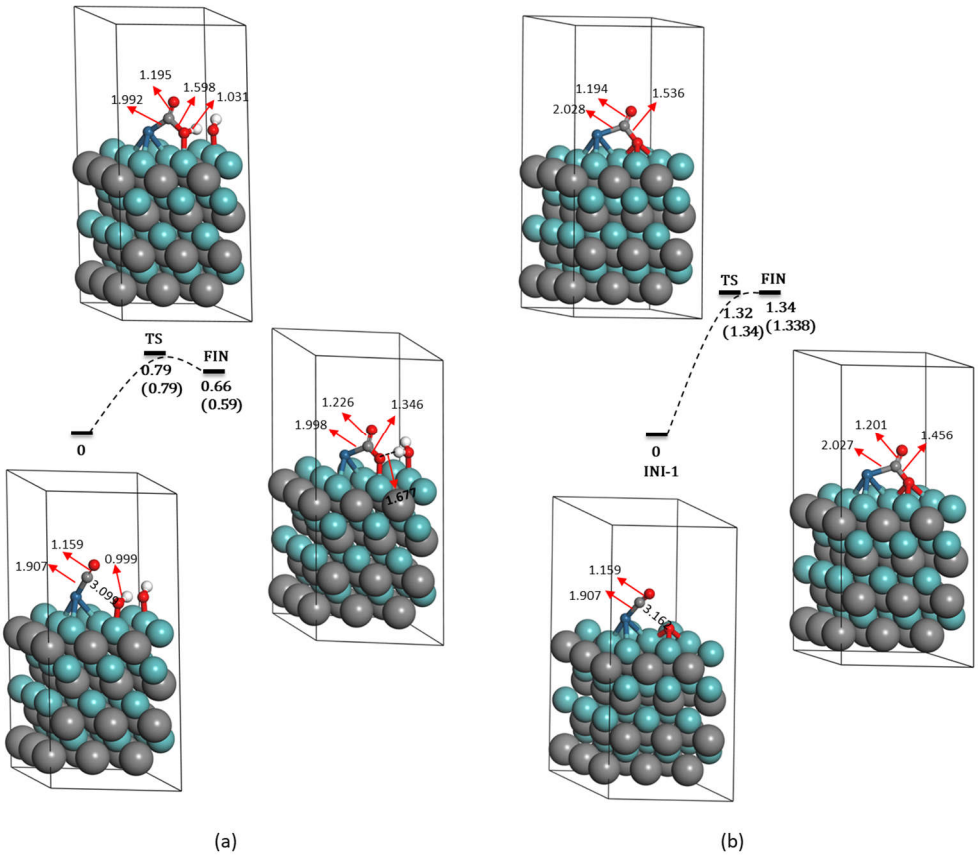

(a) (b)

Fig. S36 CO oxidation to CO_2 on Pt/MoC (111)-Mo terminated surface by surface top site OH* (a) and by surface cavity site O* (b). The adsorption of CO as energy scale reference, and energies in eV with ZPE corrections (blue ball for Pt, green ball for Mo, grey ball for C, red ball for O, white ball for H)

Table S1 Energetic aspects of surface H_2O^* dissociation with n adsorbing OH* (n = 1-3), $\Delta E_{TS,ZPE}^{\neq}$ and $\Delta E_{TS}^{\neq}$ were energy barriers of H_2O^* dissociation with or without ZPE correction, respectively; $\Delta E_{r,ZPE}$ and ΔE_r were reaction energies of H_2O^* dissociation with or without ZPE correction, respectively; σ_{TS}^{i} were imaginary frequencies of transition states for H_2O^* dissociation; $d_{O\cdots H}^{\neq}$ were the breaking O-H bond lengths of H_2O^* dissociation. Energies were in eV with H_2O^* adsorption states as reference, distances were in Å and frequencies were in cm^{-1}

			*n*HO* + H_2O^* → (*n*+1)HO* + H*			
n	$\Delta E_{TS,ZPE}^{\neq}$	$\Delta E_{TS}^{\neq}$	$\Delta E_{r,ZPE}$	ΔE_r	σ_{TS}^{i}	$d_{O\cdots H}^{\neq}$
1	0.33	0.54	−0.81	−0.67	1347	1.368
2	0.31	0.50	−0.80	−0.67	1322	1.360
3	0.24	0.43	−0.84	−0.72	1277	1.353
average	**0.29**	**0.49**	**−0.82**	**−0.69**	**1315**	**1.360**

Table S2 Energetic aspects of surface H_2O^* dissociation with n adsorbing O* (n = 1-3), $\Delta E_{TS,ZPE}^{\neq}$ and $\Delta E_{TS}^{\neq}$ were energy barriers of H_2O^* dissociation with or without ZPE correction, respectively; $\Delta E_{r,ZPE}$ and ΔE_r were reaction energies of H_2O^* dissociation with or without ZPE correction, respectively; σ_{TS}^{i} were imaginary frequencies of transition states for H_2O^* dissociation; $d_{O\cdots H}^{\neq}$ were the breaking O-H bond lengths of H_2O^* dissociation. Energies were in eV with H_2O^* adsorption states as reference, distances were in Å and frequencies were in cm^{-1}

			*n*O* + H_2O^* → *n*O* + HO* + H*			
n	$\Delta E_{TS,ZPE}^{\neq}$	$\Delta E_{TS}^{\neq}$	$\Delta E_{r,ZPE}$	ΔE_r	σ_{TS}^{i}	$d_{O\cdots H}^{\neq}$
1	0.34	0.54	−1.04	−0.89	1356	1.324
2	0.40	0.62	−0.74	−0.58	1376	1.358
3	0.37	0.59	−0.80	−0.65	1378	1.356
average	**0.37**	**0.58**	**−0.86**	**−0.71**	**1370**	**1.346**

Table S3 Energetic aspects of surface OH^* dissociation with n adsorbing O* (n = 1-3), $\Delta E_{TS,ZPE}^{\neq}$ and $\Delta E_{TS}^{\neq}$ were energy barriers of OH^* dissociation with or without ZPE correction, respectively; $\Delta E_{r,ZPE}$ and ΔE_r were reaction energies of OH^* dissociation with or without ZPE correction, respectively; σ_{TS}^{i} were imaginary frequencies of transition states for OH^* dissociation; $d_{O\cdots H}^{\neq}$ were the breaking O-H bond lengths of OH^* dissociation. Energies were in eV with OH^* adsorption states as reference, distances were in Å and frequencies were in cm^{-1}

			*n*O* + HO* → (*n*+1)O* + H*			
1	0.93	1.10	−1.14	−1.01	1501	1.339
2	0.91	1.08	−1.11	−0.98	1418	1.350
3	1.05	1.23	−0.85	−0.72	1420	1.370
average	**0.96**	**1.14**	**−1.03**	**−0.90**	**1446**	**1.353**

Table S4 Energetic aspects of surface nH_2^* dissociation (n = 1-5), $\Delta E_{TS,ZPE}^{\neq}$(The slightly negative energy barriers were due to ZPE corrections) and $\Delta E_{TS}^{\neq}$ were energy barriers of nH_2^* dissociation with or without ZPE correction, respectively; $\Delta E_{r,ZPE}$ and ΔE_r were reaction energies of nH_2^* dissociation with or without ZPE correction, respectively; σ_{TS}^{i} were imaginary frequencies of transition states for nH_2^* dissociation; $d_{O\cdots H}^{\neq}$ were the breaking O-H bond lengths of nH_2^* dissociation. The configurations of transition states at increasing H_2^* coverage were listed below the table from left to right (the breaking and forming bonds were in yellow color). Energies were in eV with nH_2^* adsorption states as reference, distances were in Å and frequencies were in cm^{-1}.

			$nH_2^* \rightarrow (n-1)H_2^* + 2H^*$			
n	$\Delta E_{TS,ZPE}^{\neq}$	$\Delta E_{TS}^{\neq}$	$\Delta E_{r,ZPE}$	ΔE_r	σ_{TS}^{i}	$d_{O\cdots H}^{\neq}$
1	−0.05	0.03	−1.03	−0.99	662	1.106
2	−0.03	0.05	−1.00	−0.97	697	1.122
3	−0.05	0.04	−0.99	−0.95	561	1.079
4	−0.04	0.04	−1.12	−1.05	412	1.041
5	−0.05	0.02	−0.79	−0.78	362	1.035
average	**−0.04**	**0.04**	**0.99**	**0.95**	**539**	**1.077**

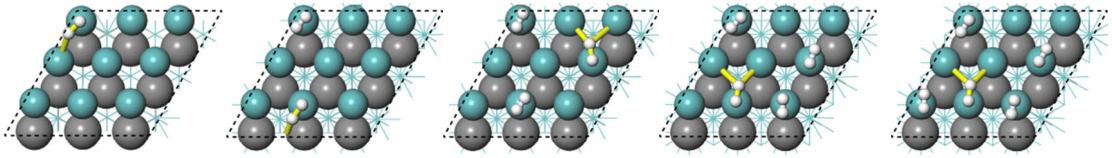

Table S5 The relative stability at 0K ($\Delta E_{AVG,n=1}^{i}$) for surface structures of H_2O^* (n = 1), OH^* (n = 1), O^* (n = 1), H^* (n = 1) with respect to H_2^* (n = 1) at increasing energy cutoff of 400, 450 and 500 eV. The differences of $\Delta E_{AVG,n=1}^{i}$ at 400 eV with those at 450 and 500 eV were also listed.

	400 eV	450 eV	500 eV	$\Delta E_{400\,eV} - \Delta E_{450\,eV}$	$\Delta E_{400\,eV} - \Delta E_{500\,eV}$
$\Delta E_{AVG,n=1}^{H2}$	0	0	0	–	–
$\Delta E_{AVG,n=1}^{H}$	−0.045 eV	−0.046eV	−0.043 eV	0.001 eV	−0.002 eV
$\Delta E_{AVG,n=1}^{H2O}$	−0.149 eV	−0.154eV	−0.153 eV	0.005 eV	0.004 eV
$E\Delta_{AVG,n=1}^{OH}$	−0.793 eV	−0.798 eV	−0.798 eV	0.005 eV	0.005 eV
$\Delta E_{AVG,n=1}^{O}$	−0.763 eV	−0.770eV	−0.772 eV	0.007 eV	0.009 eV

Table S6 Energetic aspects of surface OH* disproportionation, and energetic aspects of surface OH* direct deprotonation by surface Mo atoms.

	disproportionation	deprotonation	
n	ΔE_r	ΔE_r	$\Delta E_{TS}^{\neq}$
1	–	−0.91 eV	1.10 eV
2	–	−1.04 eV	0.96 eV
3	–	−1.07 eV	0.85 eV
4	–	−0.82 eV	0.81 eV
5	0.31 eV	−0.85 eV	0.80 eV
6	0.32 eV	−0.41 eV	1.14 eV
7	0.20 eV	−0.20 eV	1.18 eV

As pointed out in the main body, the T_d-like symmetry makes the disproportionation of adjacent cavity site OH* sterically hindered. For n $\geq$ 5, the top and bridge sites OH* emerge (**Fig. 4**), we first calculated the reaction energies of disproportionation. As shown in Table S6, at n = 5, the disproportionation between the bridge site OH* and top site OH* leading to one cavity site O* and one H_2O* is 0.31 eV endothermic, whereas the direct deprotonation of cavity site OH* by surface Mo atom leading to one cavity site O* and cavity site H* is 0.85 exothermic. In other words, the direct O-H dissociation of cavity site OH* is about 1.16 eV thermodynamically more favorable than the disproportionation pathway. Unfortunately, we couldn't target the transition state of the H transferring structure during the disproportionation process by DFT optimizations. The situations are similar for surface structures of n = 6 to 7 shown in Table S6. Thus, we could not compare the two reaction pathways through the energy barriers of transition states. We have also tried to correlate the energy barriers with reaction energies using the Bell–Evans–Polanyi (BEP) principle. Presuming that the disproportionation and direct deprotonation both comply with BEP relationship, then the energy barriers of disproportionation can be indirectly compared with those of OH* direct deprotonation. For the three points of n = 5 to 7, the energy barriers of OH* direct deprotonation by surface Mo atom show an approximately linear relationship with the reaction energies (R^2 = 0.9522). However, the BEP linear relationship disappeared when more points (n = 1 to 7) are included in the correlation. Based on the above analysis, for now, what we can say is that the OH disproportionation reaction pathway might exist at OH* surface coverage $\geq$ 5/9 ML, but it is hardly a predominant way to generate surface O* from the thermodynamic perspective.